Study of Passive Optical Network (PON)

System and Devices

Study of Passive Optical Network (PON) System and Devices

By

QINGYI GUO, M. A. Sc., B. Sc.

A Thesis

Submitted to the School of Graduate Studies

in Partial Fulfillment of the Requirements

for the Degree

Doctor of Philosophy

McMaster University

DOCTOR OF PHILOSOPHY (2013) McMaster University
(Electrical & Computer Engineering) Hamilton, Ontario

TITLE:	Study of Passive Optical Network (PON) System and Devices
AUTHOR:	Qingyi Guo, M. A. Sc. (McMaster University, Canada) B. Sc. (Peking University, China)
SUPERVISOR:	Dr. Wei-Ping Huang, Professor
CO-SUPERVISOR:	Dr. Xun Li, Professor
NUMBER OF PAGES:	xiii, 113

Abstract

The fiber-to-the-x (FTTX) has been widely investigated as a leading access technology to meet the ever growing demand for bandwidth in the last mile. The passive optical network (PON) provides a cost-effective and durable solution. In this thesis, we investigate different aspects of the PON, in the search for cost-effective and high-performance designs of link system and devices.

In Chapter 2, we propose a novel upstream link scheme for optical orthogonal frequency division multiplexing (OOFDM)-PON. The colorless laser diodes are used at the optical network units (ONUs), and the overlapped channel spectrum of orthogonal subcarrier multiplexing provides high spectral efficiency. At the optical line terminal (OLT), optical switch and all optical fast Fourier transform (OFFT) are adopted for high speed demultiplexing. The deterioration caused by the laser perturbation is also investigated.

In Chapter 3, we design a novel polarization beam splitter (PBS), which is one of the most important components in polarization-controlled optical systems, e.g. the next-generation PON utilizing polarization multiplexing. Our PBS is built on a slab waveguide platform where the light is vertically confined. Planar lenses are formed to collimate and refocus light beam by converting the phase front of the beam. A planar subwavelength grating of a wedge shape induces the form birefringence, where the transverse electric (TE) and transverse magnetic (TM) waves have different effective refractive indices, and are steered to distinct directions. This design provides low insertion loss (< 0.9 dB) and

low crosstalk (< -30 dB) for a bandwidth of 100 nm in a compact size, and can be realized by different material systems for easy fabrication and/or monolithic integration with other optical components.

In Chapter 4, we study the mode partition noise (MPN) characteristics of the Fabry-Perot (FP) laser diode using the time-domain simulation of noise-driven multi-mode laser rate equation. FP laser is cheaper than the widely used distributed feedback (DFB) laser diode in PON, but its MPN is the major limiting factor in an optical transmission system. We calculate the probability density functions for each longitudinal mode. We also investigate the k-factor, which is a simple yet important measure of MPN. The sources of the k-factor are studied with simulation, including the intrinsic source of the laser Langevin noise, and the extrinsic source of the bit pattern.

Acknowledgements

I would like to express my highest appreciation to my supervisor, Dr. Wei-Ping Huang, and my co-supervisor, Dr. Xun Li, whose guidance, support and encouragement made it possible for this work to be completed. Their diverse insights and pivotal ideas lead me to the frontier of photonics; from them, I have learnt the creativity and rigorousness in research.

I greatly appreciate the assistance I received from my committee members, Dr. Shiva Kumar, Dr. Chih-Hung (James) Chen and Dr. Chang-Qing Xu. Their constructive criticism and valuable advice on numerical and physical modeling helped me a lot in this study.

I would like to give many thanks to my colleagues in the Photonic Research Group for their friendship and fruitful discussions. I would also like to thank Ms. Cheryl Gies and other administrative staffs in the Department of Electrical and Computer Engineering for their tireless efforts and helpful attitudes.

Last but not least, I would like to thank my parents, Shucheng Guo and Kezhen Zhang, for their endless love and support in my whole life.

Table of Contents

List of Figures

List of Tables

Chapter 1.

Introduction

1.1 Background

High speed communication is always what people desire [1], [2]. Since the invention of optical fiber and erbium-doped fiber amplifier (EDFA), the optical data transmission link has advanced to the GHz regime. For the flow of information, each component in the loop has to provide a broad band in order to achieve the fast performance.

In general, there are two categories of optical communication network. One is long-haul network, which includes the submarine system, regional network and metro network. The primary factor in the long-haul network design is the overall performance of the system – high data rate, long reach and network stability to name a few. The other category is the access network, where the primary consideration factor in the network design is the overall cost of the system while aiming for better performance.

The last-mile connection of the network has been the bottleneck in a communication link due to the limited bandwidth [3]. Optical access technologies are considered to be the ideal solution to this problem, because they can offer the largest bandwidth over a maximum distance [4]. The fiber access network is often referred to as the fiber-to-the-x (FTTX), where X stands for the location of the fiber termination, e.g. H

for home, C for curb, and B for building. Instead of point-to-point architectures, the passive optical network (PON) utilizes point-to-multiple-point architecture. The optical line terminal (OLT) is at the central office, and the optical network unit (ONU) is at each subscriber node. Thus, the PON provides a cost-effective, bandwidth-management flexible, scalable and durable solution to the ever growing demand for bandwidth in the last mile.

There are several different schemes to utilize the PON architecture: time division multiplexing (TDM)-PON [5], [6], wavelength division multiplexing (WDM)-PON [7], [8], optical code division multiplexing (OCDM)-PON [9], [10], subcarrier multiplexing (SCM)-PON [11], [12], orthogonal frequency division multiplexing (OFDM)-PON [13], [14], etc.

Among these schemes, TDM-PON and WDM-PON are regarded as the mainstream realizations of the optical access network, and have been employed commercially.

There are a few TDM-PONs standardized by IEEE and ITU-T. Based on the IEEE 802.3ah standard, gigabit Ethernet PON (EPON) supports downstream and upstream speeds of up to 1.2 Gbit/s and up to 32 ONUs, with a maximum distance of 20 km [15]. Based on the ITU-T G.984 standard, gigabit-capable PON (G-PON) offers asymmetrical service with 2.5 Gbit/s downstream transmission and 1.25 Gbit/s upstream, and supports for up to 64 ONUs and a maximum distance of 60 km [16]. Recently, 10 Gbit/s PON systems have been standardized, including the 10G EPON by IEEE 802.3av standard [17], and XG-PON by ITU-T G.987 standard [18]. In these systems, the

downstream speed can achieve 10 Gbit/s, and the upstream speed has options from 1 Gbit/s or 2.5 Gbit/s, and 10 Gbit/s. TDM is used as the multiplexing scheme between the OLT and ONUs in these systems. WDM is used in the gigabit-class and 10 gigabit-class PON systems for directional multiplexing and service multiplexing, e.g. to multiplex upstream and downstream signals, and to multiplex video signals onto data signals [19]. WDM is also used to multiplex different PON systems, such as to split and combine GPON and 10 Gbit/s GPON.

New WDM related PON systems have been studied for the next generation scalable and flexible PONs [19]. One category is WDM-PON, where each ONU uses a unique wavelength in each direction to communicate with the OLT. The other category is combined WDM/TDM-PON, where several wavelengths are used to communicate between OLT and ONUs, and each wavelength is shared by a few ONUs by TDM. WDM related PON systems not only can offer higher speed than TDM-PONs, but also can excel in scalability and information security. However, they are more costly compared to TDM-PONs.

Optical orthogonal frequency division multiplexing emerged recently for its high speed and spectral efficiency compared with TDM and WDM, and extreme robustness against chromatic dispersion and polarization mode dispersion [20], [21]. Therefore, OFDM-PON has been proposed and investigated intensively [22], [23].

Advanced PON architectures have been actively pursued to achieve a high transmission rate. A recent PON architecture utilizing OFDM, polarization multiplexing (POLMUX), 16- quadrature amplitude modulation (QAM) scheme and direct detection

enables 108 Gbps data rate on a single wavelength for 20 km transmission [24]. This architecture combines several different multiplexing and modulation schemes, and is regarded as an attractive candidate for next-generation optical access network.

In the markets of FTTX, the emphasis on technologies includes two aspects: "farther and faster", and "more and cheaper". Intensive research and development efforts have been carried out to pursue high-volume and low-cost components such as optical transceivers, multiplexers/demultiplexers, and splitters/combiners.

The conventional optical modules are based on optical subassemblies, which are made of discrete chips [4]. For example, chips of distributed feedback (DFB) laser diodes and PIN photo diodes are packaged into TO-cans, which are assembled into optical subassemblies, and mounted onto printed circuit boards (PCBs) with other microelectronic chips to form an optical transceiver module. New hybrid and monolithical integration technologies have emerged to reduce the discrete components, thus to increase the production throughput and reduce the overall cost. The chip-level integration is the ultimate goal, where the photonic devices are connected monolithically or hybridly to form a single and rugged photonic integrated circuit. Different material platforms will be appropriate for different purposes: InP for optical only integration; GaAs for both the optical and electronic components/circuitry; and Si-based platform if lighted externally.

The laser diode is the key element used at both OLTs at the central office and ONUs at each subscriber's premises. Due to the serious dispersion-related impairments, costly narrow-linewidth lasers, such as DFB laser diodes, are needed. Much attention has

been paid to find the low-cost alternative to the DFB laser, e.g. a single mode Fabry-Perot (FP) laser made by etching a few shallow slots on the ridge [25]. Conventional FP lasers are also studied for the application in 10 Gbit/s transmission uplinks. An InGaAlAs multi-quantum-well (MQW) FP laser is experimentally shown for 4 km transmission at 10 Gbit/s over a temperature range from 0 to 85 ℃ [26]. In another scheme, forward-error correction (FEC) can offer an effective optical gain higher than 2.7 dB for a 1.25 Gbit/s burst-mode GPON uplink using FP laser, and the reach is equivalently over 12 km [27].

1.2 Thesis Outline

In this thesis, I will explore different aspects of the PON, in the search for cost-effective and high-performance designs of link system and devices.

In Chapter 2, we propose a novel optical orthogonal frequency division multiplexing (OOFDM)-PON upstream link scheme. We first review the advantages and disadvantages of WDM and OFDM in the introduction section. The architecture of our proposed link and its working principle are demonstrated in the second section. At the ONUs, orthogonal subcarrier multiplexing is used to realize colorless ONU and high spectral efficiency. At the OLT, the optical switch and all optical FFT are applied to achieve high speed demultiplexing. In the third section, numerical simulations are conducted with two configurations: 10 Gbit/s bit rate for 4 ONUs, and 2.5 Gbit/s bit rate for 16 ONUs. According to the Monte-Carlo simulation results of the BER, the tolerance

of the laser diode central wavelength shift in ONUs for 10 Gbit/s link is higher than that for the 2.5 Gbit/s link. The last section summarizes this chapter.

In Chapter 3, we design a novel polarization beam splitter (PBS) on a slab waveguide platform where the light is vertically confined. In the introduction section, we review and compare state-of-the-art PBS designs. In the second section, the structure of our proposed PBS and its fundamental working principle are described, with a brief explanation of form birefringence and diffractive optics. Planar lenses are formed to collimate and refocus light beam by converting the phase front of the beam. A planar subwavelength grating of a wedge shape induces the form birefringence, where the transverse electric (TE) and transverse magnetic (TM) waves have different effective refractive indices, and are steered to distinct directions. In the third section, the detailed design procedure and considerations are provided, including the calculation of material and effective indices, lens design, wedge and waveguide design. In the fourth section, the simulation setup and results are shown. This design provides low insertion loss (< 0.9 dB) and low crosstalk (< -30 dB) for a bandwidth of 100 nm in a compact size, and can be realized by different material systems for easy fabrication and/or monolithic integration with other optical components. Finally, a summary concludes this chapter in the fifth section.

In Chapter 4, we investigate the mode partition noise (MPN) characteristics of Fabry-Perot laser diode using the time-domain simulation of noise-driven multi-mode laser rate equation. In the introduction section, the previous works on the study of MPN are reviewed, including the theoretical analysis, experimental measurements, and

suppression schemes of MPN. In the second section, the model of multimode rate equations with Langevin noise terms is illustrated. The mode probability density functions (pdfs) and k-factors are briefly described in the third section. In the fourth section, we demonstrate the numerical simulation setup, and show the simulation results for the mode pdfs and k-factors. The sources of the k-factor are studied, including the intrinsic source of the laser Langevin noise, and the extrinsic source of the bit pattern. The fifth section summarizes this chapter.

Finally, I will give the summary of this thesis, and discuss possible future works in Chapter 5.

Chapter 2.

A Novel Upstream Link Scheme for OOFDM-PON

2.1 Introduction

As reviewed in Chapter 1, fiber-to-the-x (FTTX) has been widely investigated as a leading access technology to meet the ever growing demand for bandwidth in the last mile, and PON is regarded as a cost-effective and durable solution.

WDM-PON is a promising candidate for the next-generation access network due to its high speed, scalability in terms of bandwidth and wavelengths, flexibility and security. Figure 2-1 shows a typical configuration of WDM-PON system. A simple way to realize WDM-PON is to employ a different laser with a specific wavelength in each ONU. However, this increases the inventory and maintenance burden of the network operation [19]. Therefore, how to implement colorless ONU, where wavelength is independent, has been a major issue and research focus [28], [29]. Another inherent problem with WDM-PON is that the channels are non-overlapped with guard bands in between, as shown in Figure 2-2 (a), leading to a wider bandwidth than actually required. And at the receiver end, tuned analog filters are needed to separate the subcarriers.

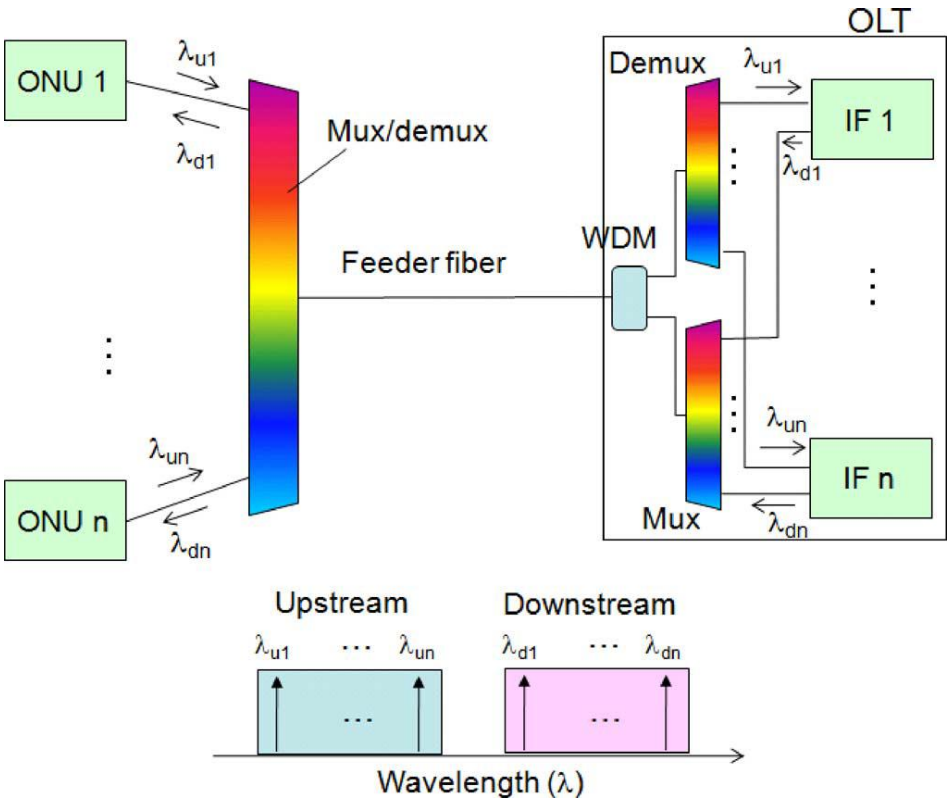

Figure 2-1 A typical configuration of WDM-PON system [19].

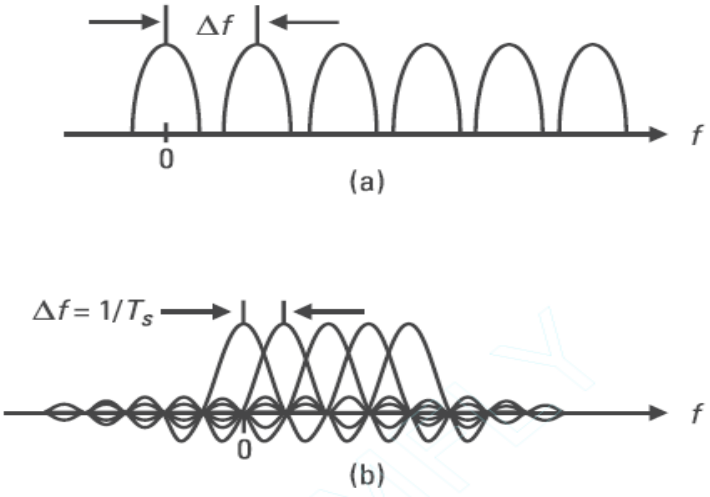

Figure 2-2 Spectra for (a) WDM signal and (b) OFDM signal.

Orthogonal frequency division multiplexing (OFDM) has been used vastly in broadband wireless and wired communication systems [30], [31], and has attracted intensive research interest in optical communications [32]-[38]. It is one class of multi-carrier modulation (MCM) [21], but information data are carried on orthogonal subcarriers with overlapped spectrum, as shown in Figure 2-2 (b). The input serial data is first converted to parallel data streams, where the symbol period is longer, and then transmitted on a number of different frequencies. The subcarriers can utilize conventional modulation schemes, such as on-off keying (OOK), phase-shift keying (PSK), and quadrature amplitude modulation (QAM).

One advantage of OFDM is the high spectral efficiency as compared with WDM, as shown in Figure 2-2. The orthogonality of subcarriers over one OFDM symbol period guarantees that the signal can be recovered without inter-channel interference (ICI) at the demodulator. And the modulation and demodulation can be implemented by inverse discrete Fourier transform (IDFT) and discrete Fourier transform (DFT) [39], and these can be efficiently implemented by fast Fourier transform (FFT) with the digital electronic circuits. Another advantage of OFDM is that it can mitigate the inter-symbol interference (ISI) and ICI induced by chromatic dispersion and polarization mode dispersion (PMD), because of the longer symbol period and the added cyclic prefix [30], [40].

One drawback of OFDM is that it is sensitive to frequency offset and phase noise, because this would affect the orthogonality of subcarriers and lead to ICI and ISI. OFDM can have a high peak-to-average power ratio (PAPR) when the independently modulated subcarriers add up constructively at a certain time. The high PAPR may suffer from the

nonlinearity in the optical link, e.g. fiber nonlinearity [42]-[46], and this would deteriorate the subcarrier orthogonality. Therefore, OFDM is a promising technique for high data rate transmission over a short range, where nonlinearity is negligible. As an example, at the wavelength of 1.55 μm, for standard telecommunication fibers, the nonlinear effect is negligible for a fiber length of 50 km if the pulse width is 100 ps and peak launch power is 1 mW [47]. PON is an access network with negligible nonlinearity, thus suitable for OFDM application. OFDM-PON has a better performance than TDM-PON, and is cheaper than WDM-PON.

In this chapter, we propose a novel upstream link scheme for optical orthogonal frequency division multiplexing (OOFDM)-PON. The architecture and working principle of the proposed scheme is illustrated in the second section. The colorless laser diodes are used at the optical network units (ONUs), and the overlapping channel spectrum of orthogonal subcarrier multiplexing provides high spectral efficiency. At the optical line terminal (OLT), optical switch and all optical fast Fourier transform (OFFT) are adopted for high speed demultiplexing. Numerical simulations for two link configurations, i.e. 10 Gbit/s bit rate for 4 ONUs, and 2.5 Gbit/s bit rate for 16 ONUs, are shown and analyzed in the third section. The chapter is summarized in section 4.

2.2 Architecture and Working Principle

Figure 2-3 shows the conceptual diagram for our proposed scheme for the upstream link of the OOFDM-PON.

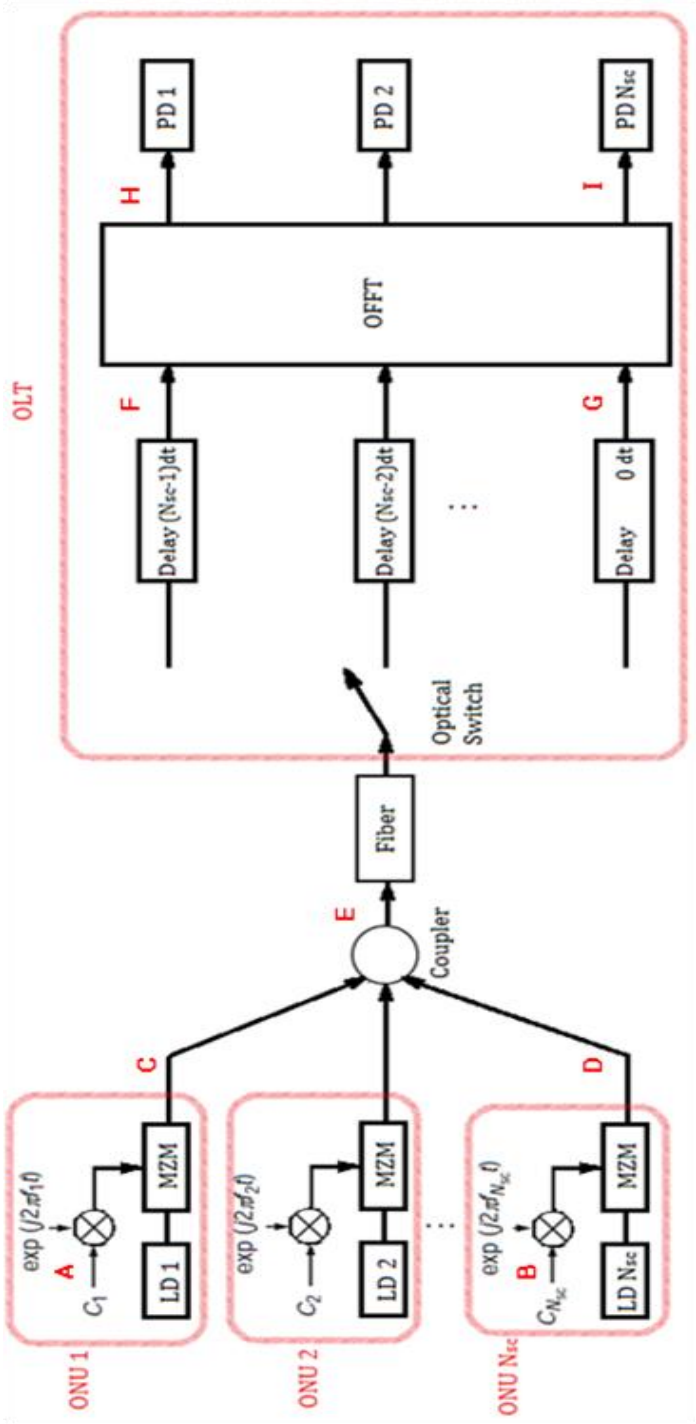

Figure 2-3 The conceptual diagram for OOFDM-PON.

At the ONUs, the orthogonal subcarrier multiplexing is utilized. The signal carried on each subcarrier is the information bits from each ONU, instead of the parallel data streams converted from one serial input data stream in the traditional OFDM architecture. The information bit train $c_k\left(k=1,2,\cdots,\ N_{sc}\right)$, where N_{sc} is the total number of ONUs, is mixed by a subcarrier frequency f_k in the electronic domain. The continuous wave from the single-mode laser diodes (LDs), e.g. distributed feedback (DFB) LDs, are modulated by the electrical signal via the Mach-Zehnder modulator (MZM) module, and a simple optical coupler combines optical signals from each ONU. The external modulation of DFB LD using MZM can also be replaced with a directly-modulated DFB LD, which will further reduce the cost.

The transmitted signal can be expressed as [21]

$$s(t)=\sum_{i=-\infty}^{\infty}\sum_{k=1}^{N_{sc}}c_{ki}s_k\left(t-iT_s\right) \tag{2.1}$$

where c_{ki} is the *i*-th information bit on the *k*-th subcarrier, T_s is the symbol period, and s_k is the waveform of the *k*-th subcarrier:

$$s_k(t)=\Pi(t)\exp\left(j2\pi f_k t\right) \tag{2.2}$$

Here $\Pi(t)$ is the pulse shaping function. In this chapter, we simply use non-return-to-zero (NRZ) coding and square pulses, and then $\Pi(t)$ is the gate function:

$$\Pi(t)=\begin{cases}1, & \left(0<t\le T_s\right)\\ 0, & \left(t\le 0,\ t>T_s\right)\end{cases} \tag{2.3}$$

The inner product of two subcarriers can be written as

$$\begin{aligned}\frac{1}{T_s}\int_0^{T_s} s_k s_l^* \delta t &= \frac{1}{T_s}\int_0^{T_s} \exp\left[j2\pi\left(f_k - f_l \right)t \right]\delta t \\ &= \exp\left[j\pi\left(f_k - f_l \right)T_s \right]\mathrm{sinc}\left[\pi\left(f_k - f_l \right)T_s \right]\end{aligned} \tag{2.4}$$

If the subcarriers are spaced at frequencies that are multiples of the inverse of the bit duration

$$f_k - f_l = m\frac{1}{T_s}, \quad m \text{ is integer} \tag{2.5}$$

Eq. (2.4) becomes zero, and the two subcarriers are orthogonal. Here we place the subcarrier frequencies at:

$$f_k = \frac{k-1}{T_s} \tag{2.6}$$

At the OLT, an optical switch allocates sequentially the corresponding time slots of the pulses to each channel. The duration of each time slot is

$$dt = \frac{T_s}{N_{sc}} \tag{2.7}$$

This is equivalent to sampling the received signal at every interval of *dt*. For the simple back-to-back case, the received signal is the transmitted signal, and its *i*-th symbol is $s_i(t)$. The *m*-th sample of the *i*-th symbol can be written as

$$\begin{aligned} s_{im} &= \sum_{k=1}^{N_{sc}} c_{ki} \exp\left[j2\pi f_k \frac{(m-1)T_s}{N_{sc}} \right] \\ &= \sum_{k=1}^{N_{sc}} c_{ki} \exp\left[j2\pi \frac{(k-1)(m-1)}{N_{sc}} \right] \\ &= F^{-1}\{c_{ki}\} \end{aligned} \tag{2.8}$$

where $F^{-1}\{\cdot\}$ is the inverse Fourier transform, and m = 1, 2, …, N_{sc}. Therefore, the demultiplexer in the form of Fourier transform can recover the input information symbols perfectly. If the transmission has chromatic dispersion and/or polarization mode dispersion, the addition of cyclic prefix can mitigate the problem, and the above analysis still holds.

From the DFT expression, we can see that it is actually just controlled phase delays and power couplers. Therefore, the optical FFT (OFFT) components have been implemented using star couplers and phase adjustments [45]. An OFFT circuit design combining optical delays and phase shifters was applied to a 4×25 Gbit/s transmission using numerical simulations [46]. A simpler implementation of OFFT device was realized by combining the serial to parallel (S/P) conversions and optical delays and couplers into one, and by re-ordering the delays and re-labeling the outputs [48], [49]. By encoding 4 odd channels with differential phase-shift keying (DPSK) data at 28 GBd and 5 even channels with differential quadrature phase shift keying (DQPSK) data, a 392 Gbit/s OFDM signal transmission is realized.

The OFFT differs from the electronic FFT that it operates continuously; thus, all the N_{sc} time samples in one symbol period T_s must be fed simultaneously into the OFFT

circuit. Therefore, at the OLT, the sampled pulses in the time slot *dt* at each channel are delayed by $(N_{sc}-1)dt$, $(N_{sc}-2)dt$, ..., $1dt$, $0dt$, respectively. Then the pulses are fed to an all optical fast Fourier transform (OFFT) processor for demultiplexing, and finally received by photo diodes (PDs).

The merit of using OFFT device instead of electronic FFT is that the demultiplexing of the OFDM subcarriers can be done optically with high speed, and only the subcarrier signal processing is to be done in the electronic domain. Thus, the speed limit imposed by the capabilities of the electronic receivers is greatly relaxed to the subcarrier data rate.

In our proposed scheme of OOFDM-PON, the laser diodes of the ONUs are colorless, and therefore, they are interchangeable and cost-effective. The demultiplexing by OFFT is operated in the optical domain; thus, a higher symbol rate can be achieved compared to demultiplexing in the electronic domain. The reason why we do not use optical inverse FFT (OIFFT) for multiplexing at the ONUs is that, in order to combine the pulse train from each ONU, the pulse width has to be *dt*, which not only put a stringent requirement for the lasers, but also increases greatly the baseband bandwidth [46].

2.3 Link Simulation and Results

We numerically simulate the 1310 nm upstream link for two configurations: nominal bit rates of 2.5 Gbit/s for 16 ONUs, and 10 Gbit/s for 4 ONUs. NRZ pulses are used as the baseband waveform. We consider linear fiber in the PON.

The illustrative points in the OOFDM-PON architecture are marked with letters A to I in Figure 2-3, and the baseband waveforms at those points for the configuration of 10 Gbit/s for 4 ONUs are shown in the corresponding figures. Figure 2-4 shows the waveform of the information bits directly from the 1st and N_{sc}-th home, at points A and B. Figure 2-5 shows the waveform after the MZMs in the 1st and N_{sc}-th ONUs, at points C and D. Figure 2-6 is the waveform of the combined signals from all the ONUs at point E, and Figure 2-7 illustrates its optical spectrum. As shown, the spectra of subcarriers overlap with each other, and are orthogonal so that the subcarriers have no impact on others. Figure 2-9 shows the waveforms in the OLT, after the optical switch and proper delays, at points F and G. Figure 2-10 shows the waveforms after the OFFT in blue lines, i.e. the outputs of the demultiplexer, at points H and I. Also shown is the input bit trains from the subscribers at points A and B in black lines. We can see that the information bits are recovered at the end of the link system, and the pulse durations are shortened to $1/N_{sc}$ of the original symbol period. Figure 2-8 illustrates the transmitted overlapping optical spectrum for the configuration of 2.5 Gbit/s with 16 ONUs.

The major performance degradation of the proposed OOFDM-PON comes from the frequency shift and phase noise of the laser diodes in ONUs. Here, the bit error rate

(BER) is studied as a function of the central frequency shift of the laser diodes in ONUs by Monte-Carlo method. The frequency shift is modeled by a Gaussian distribution with zero mean and standard deviation of σ_f, while the initial phase of the laser diodes is uniformly distributed between 0 and 2π. The BER results are shown in Figure 2-11.

The central frequency shift of the laser diodes deteriorates the orthogonality of the subcarriers; therefore, the configuration with higher bit rate can tolerate a larger frequency shift of laser diodes. As shown in Figure 2-11, for the same amount of the central frequency shift, the 10 Gbit/s link has a lower BER than the 2.5 Gbit/s link. For the forward error correction (FEC) limit of 10^{-3}, the standard deviations of laser central frequency are approximately 0.2 GHz for 2.5 Gbit/s configuration, and 0.6 GHz for 10G bit/s configuration. Besides, the splitting loss of the optical coupler for 16 ONUs is larger than that for 4 ONUs. Therefore, the configuration of 10 Gbit/s link with 4 ONUs has a better overall performance than the 2.5 Gbit/s link with 16 ONUs.

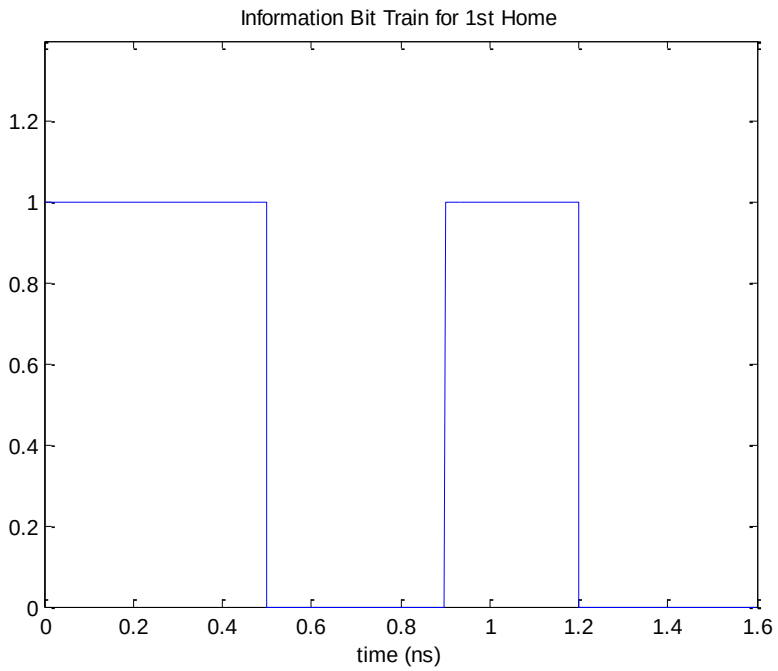

A

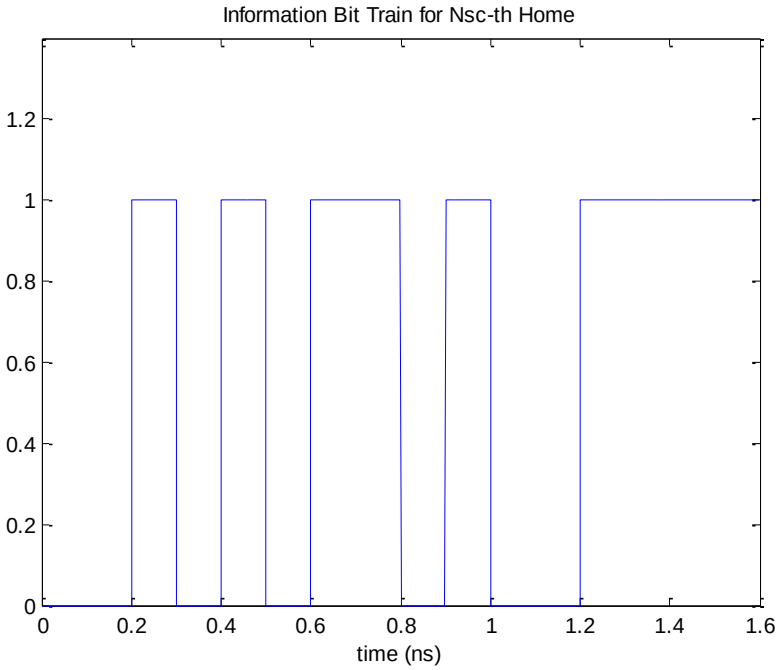

B

Figure 2-4 Baseband waveforms of the information signals at ONUs, at points A and B.

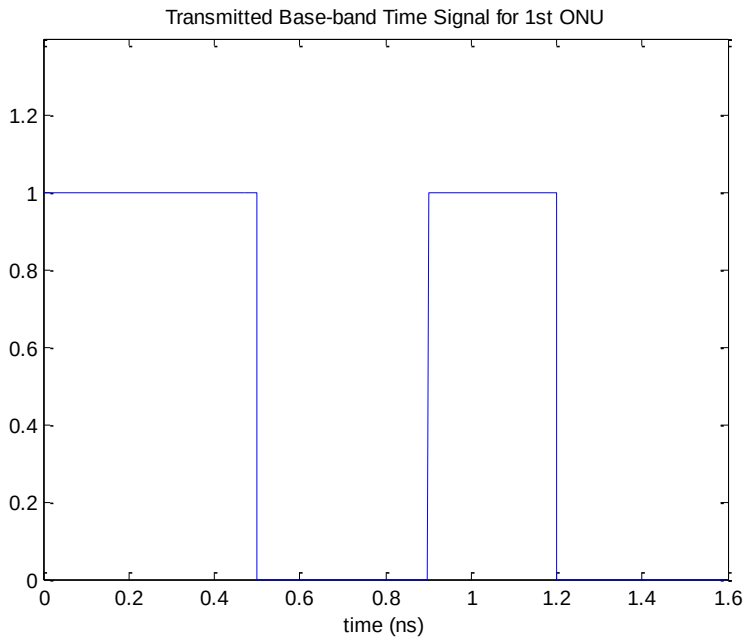

C

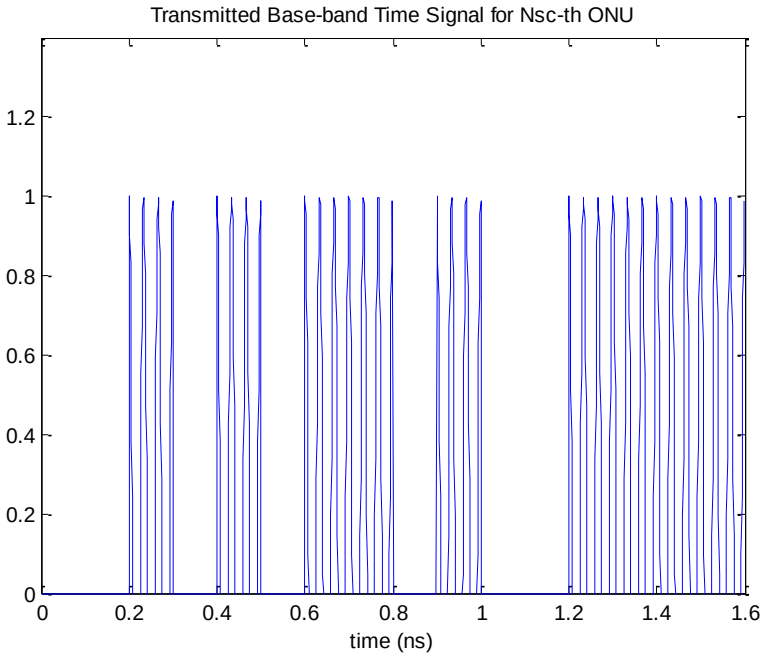

D

Figure 2-5 Baseband waveforms of the information signals at ONUs, after MZMs at points C and D.

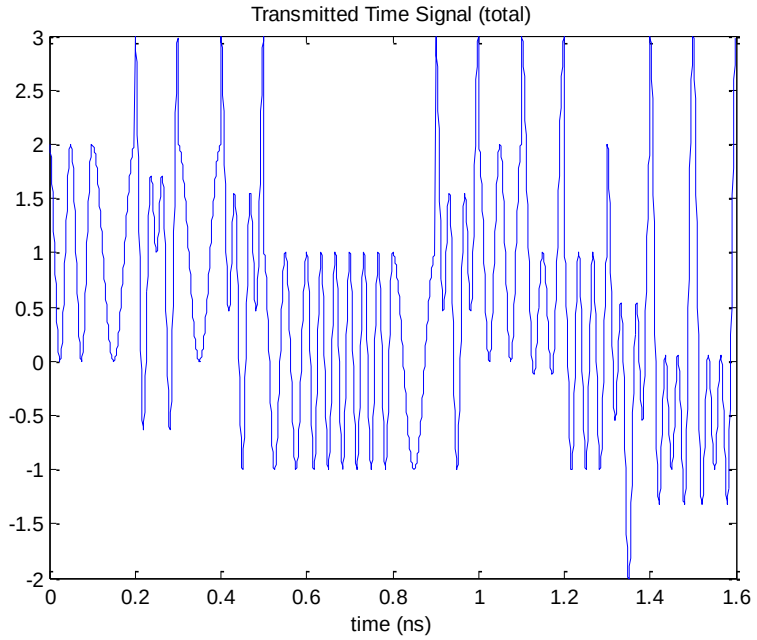

E

Figure 2-6 Baseband waveform of the information signals after the coupler, at point E.

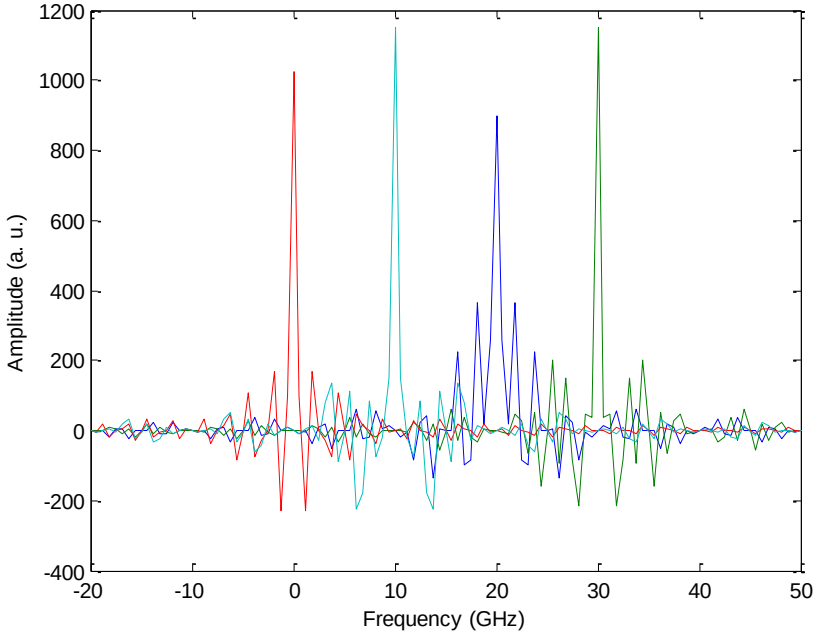

Figure 2-7 Transmitted optical spectrum for 10 Gbit/s for 4 ONUs.

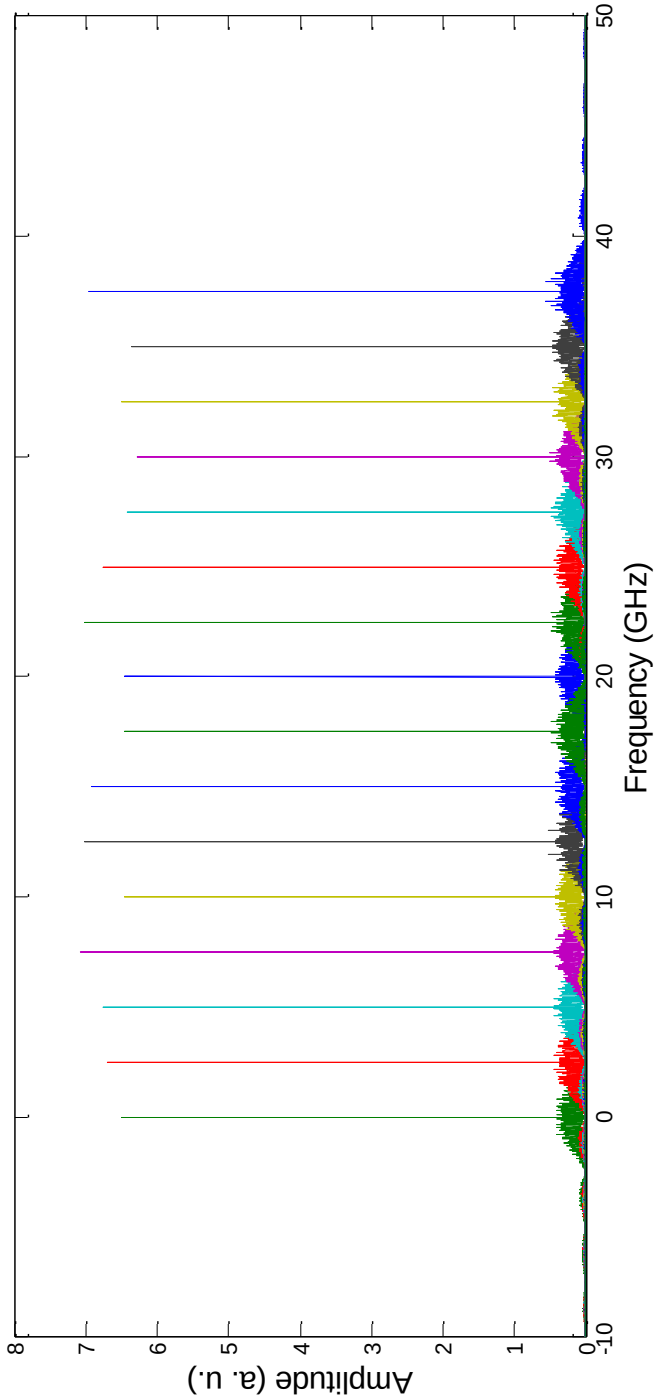

Figure 2-8 Transmitted optical spectrum for 2.5 Gbit/s for 16 ONUs.

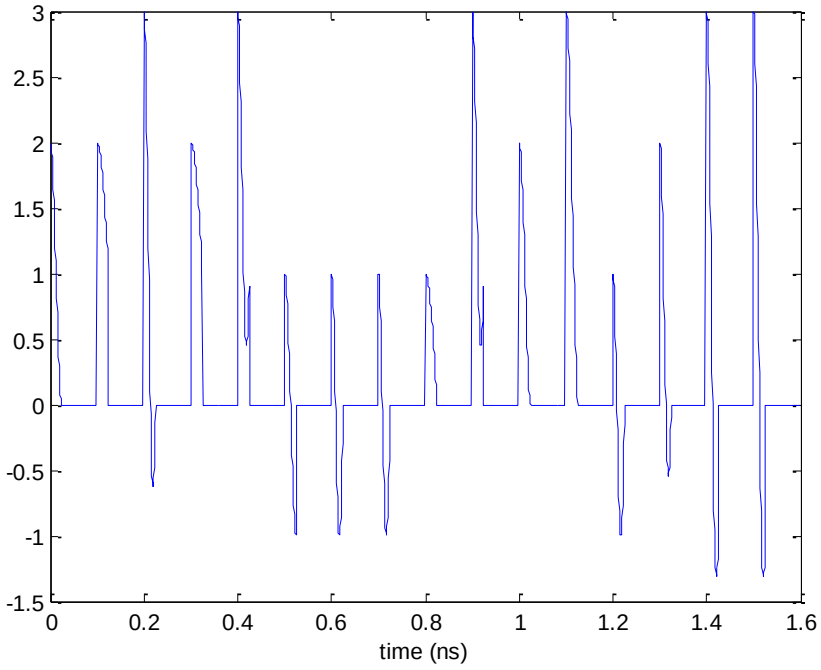

F

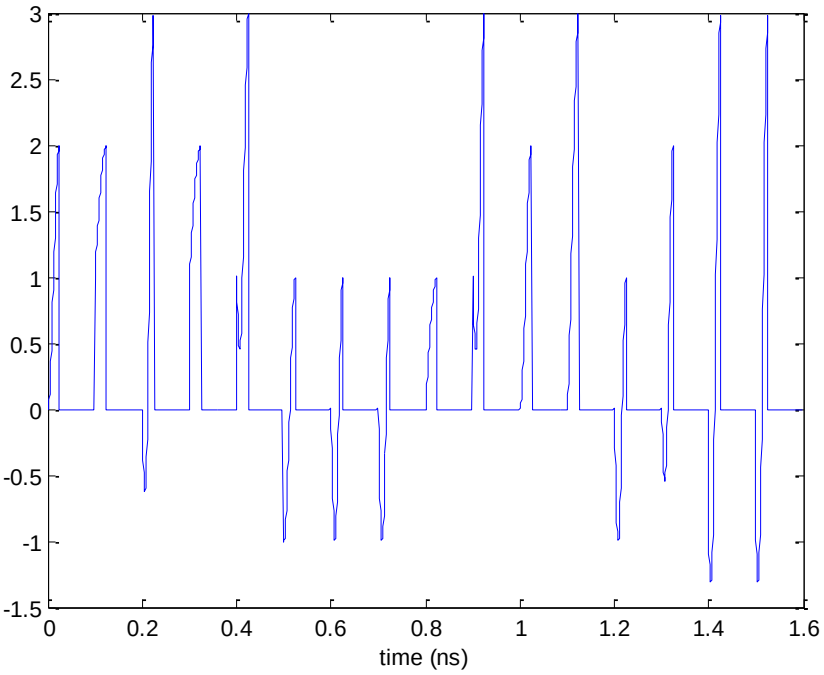

G

Figure 2-9 Baseband waveforms of the information signals in OLT, at points F and G.

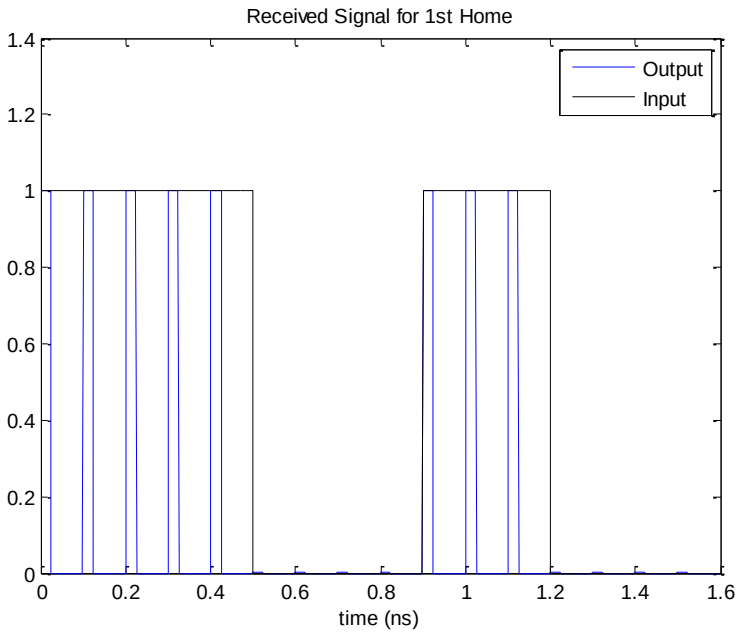

H

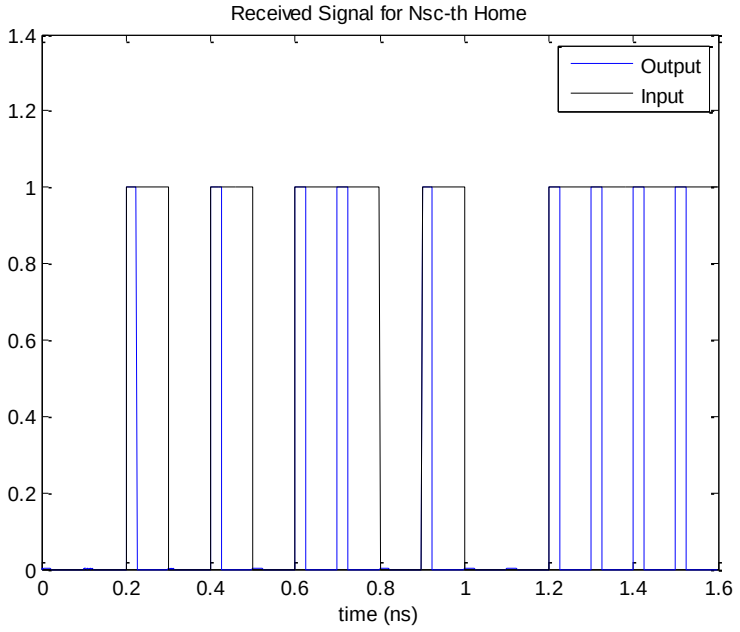

I

Figure 2-10 Baseband waveforms of the output signals after OFFT at the OLT, at points H and I (blue lines). The input waveforms are also shown for comparison in black lines at points A and B.

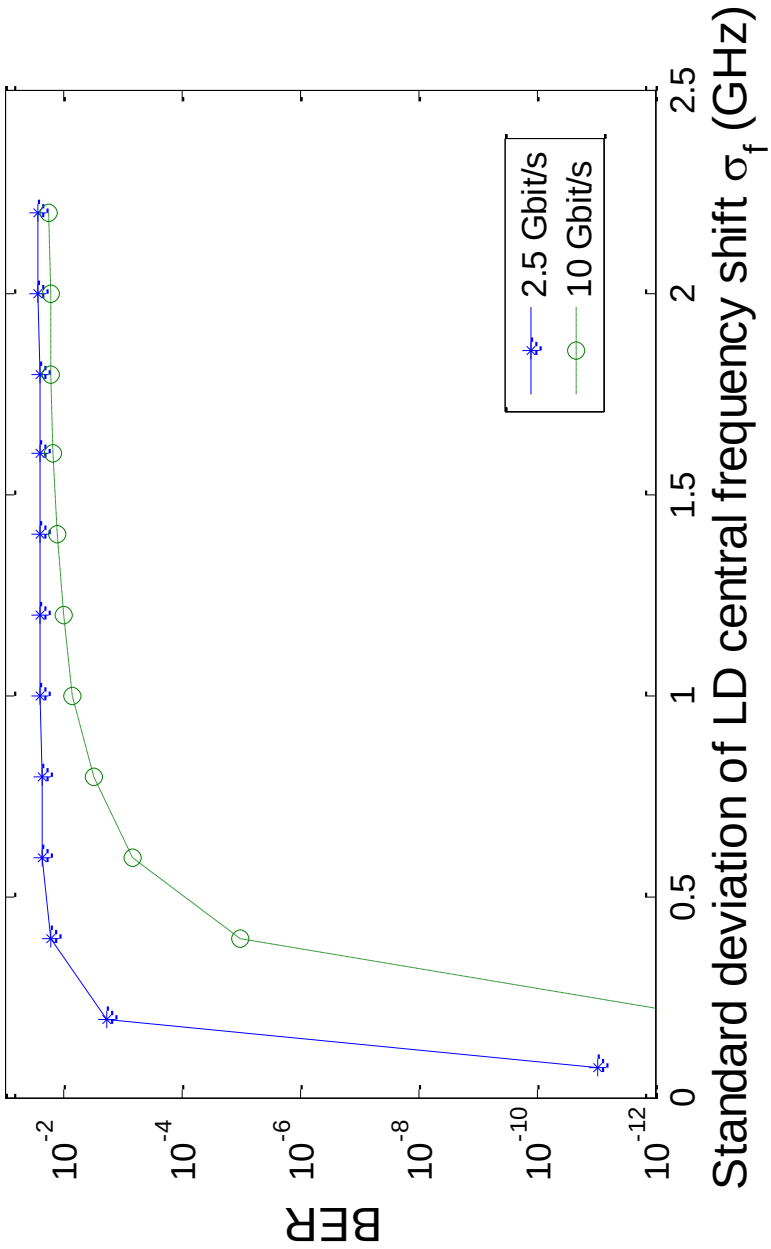

Figure 2-11 BER as a function of the central frequency shift of the laser diodes in ONUs.

2.4 Summary

A novel OOFDM-PON upstream link scheme is proposed and numerically simulated with two configurations: 10 Gbit/s bit rate for 4 ONUs, and 2.5 Gbit/s bit rate for 16 ONUs. At the ONUs, orthogonal subcarrier multiplexing is used to realize colorless ONU and high spectral efficiency. At the OLT, the optical switch and all optical FFT are applied to achieve high speed demultiplexing. According to the Monte-Carlo simulation results of the BER, the tolerance of the laser diode central wavelength shift in ONUs for 10 Gbit/s link is higher than that for the 2.5 Gbit/s link.

Chapter 3.

Planar Waveguide Polarization Beam Splitter Based on the Form Birefringence

3.1 Introduction

Polarization beam splitters (PBSs) are one of the most important components in polarization-controlled optical systems, e.g., polarization multiplexed long-haul fiber-optic communication systems, and next-generation passive optical network (PON) based on polarization multiplexing [24].

There are two categories of PBSs. One is discrete PBS, and some of the examples are conventional PBS such as Wollaston prism, and form-birefringent PBS [50], [51]. These designs can be broadband with low loss and low crosstalk, but cannot be easily integrated with other optical components. The other category is integrated PBS, which can be further classified into the interference type [52]-[55] and the mode evolution type [56]. Devices based on interference effect [52]-[55] have short device lengths and low loss, but their extinction ratio (ER) is relatively low and the bandwidth is usually small. A variety of waveguide structures that these PBSs are built on provide potential compatibility with different optical components. Devices based on mode evolution suppress mode coupling, thus have a broadband with low loss and high ER in a compact

size [56], but they are not directly integratable with planar waveguide based devices.

In this chapter, we propose a novel PBS design that has features comparable to the state-of-the-art devices. Besides, our device is based on a planar waveguide platform, and therefore can be monolithically integrated with other optical components built on the same platform [57], [58]. The form birefringence provides an enlarged effective index difference between the TM and TE polarizations over a broad bandwidth. The device shown in this letter is based on a silicon-on-insulator (SOI) material system. Simulation results show that, with a size of 300 μm × 80 μm, its crosstalk can be less than -30 dB with insertion loss under 0.9 dB for a wavelength range from 1.5 μm to 1.6 μm.

Comparison between the suggested structure and the previously reported beam splitters can be made in terms of compatibility (for monolithic integration), insertion loss, crosstalk or extinction ratio, size, and bandwidth. The comparison can be summarized in Table 3-1, and the details of the references of the integrated PBSs [52]-[56] are summarized in Table 3-2.

In this chapter, we first describe the structure of our proposed PBS and its fundamental working principle, with a brief explanation of form birefringence and diffractive optics. Next, we provide the detailed design procedure and considerations, including the calculation of material and effective indices, lens design, wedge and waveguide design. Then, we describe briefly the simulation setup, and show the simulation results of field distribution, insertion loss and crosstalk. The PBS performance in the band between 1.5 μm and 1.6 μm is studied. Finally, a summary concludes this chapter.

Table 3-1 Comparison between the proposed PBS and previously reported PBSs.

Type	Insertion Loss	Crosstalk	Bandwidth	Size	Integration
Discrete	✓	✓	✓	✓	×
Integrated: Interference	✓	×	×	✓	✓
Integrated: Mode Evolution	✓	✓	✓	✓	×
Proposed	✓	✓	✓	✓	✓

Table 3-2 Comparison between the proposed PBS and references of integrated PBSs.

Ref #	Size	Insertion Loss	Extinction Ratio	Bandwidth	Structure
[52]	length = 46.7μm	~ 0	22 dB	18 nm: ER > 20 dB	two horizontally slotted waveguide (SOI)
[53]	7 μm × 16 μm	< 0.5 dB	15 dB (single), > 20 dB (double)	1.5 - 1.6 μm: ER > 12 dB (TE), ER > 6 dB (TM)	silicon wire
[54]	length = 200 μm	3 dB (TM)	15 dB	at 1.31 and 1.55 μm, ER > 15 dB	tapered metal line
[55]	20 μm × 7 μm	Transmission: 30% TM, 10% TE		1.25 – 1.3 μm	planar photonic crystal
[56]	length = 200 μm	~ 0	> 30 dB (at 1.63μm)	1.45 – 1.75 μm ER > 22 dB	two high-index-contrast dielectric waveguide
Pro-posed	300 μm × 80 μm	< 0.9 dB	Crosstalk < -30 dB	1.5 - 1.6 μm	planar waveguide platform, form birefringence

3.2 Structure and Working Principle

3.2.1 Structure

A schematic structure of our proposed PBS design is shown in Figure 3-1. The light is vertically confined (along the *x* direction) by the SOI slab waveguide in the *x*-*y* plane [57]. By three etching steps, the top layer can be etched with different thicknesses, as shown in the inset of Figure 3-1. Mesas with different heights are formed, where large heights provide high effective refractive indices. In Figure 3-1, area D is the platform background. Area A's are input – output waveguides. Area B's are lenses designed to collimate and refocus light beams. Area C is a wedge constructed by a subwavelength grating, where two strip mesas with effective refractive indices n_h and n_l are stacked along the *y* direction.

3.2.2 Form Birefringence

From the effective medium theory, when the subwavelength grating period Λ is much smaller than the light wavelength λ, the grating can act as homogeneous birefringent material [59]. For the TM polarized wave, the electric field **E** is along the *x* axis, and is continuous at the grating boundaries. Thus, the effective refractive index of the grating area is simply the weighted average of the high-part index and low-part index for the TM wave. For the TE wave, **E** is along the *y* axis, and the displacement field $n^2\mathbf{E}$ is continuous at the grating boundaries. Compared to the TM wave, a larger portion of the TE wave's electric field resides in the low-index part; therefore, the effective refractive index of the TE wave is lower than that of the TM wave in the grating area.

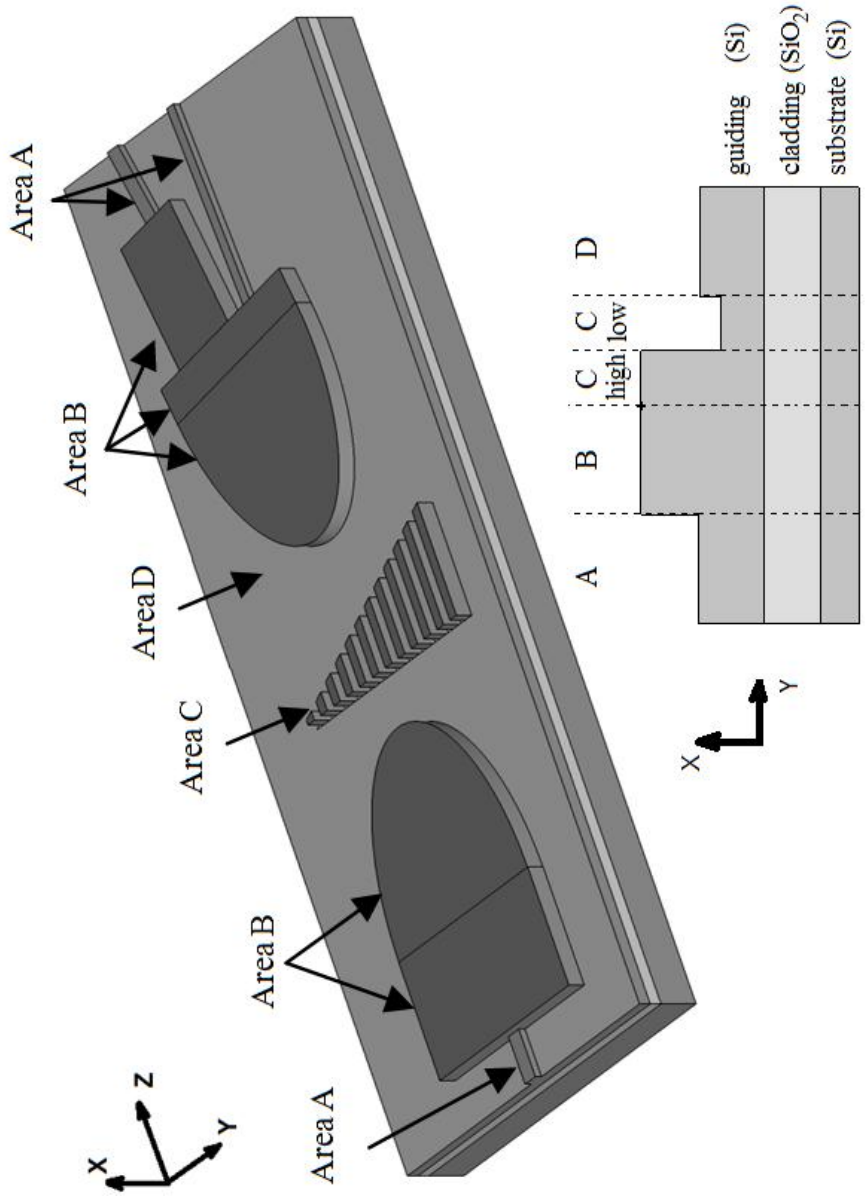

Figure 3-1 Schematic structure of the proposed PBS. Inset: Cross section view of the slab waveguides for different areas.

In this chapter, we also use X-polarization (X-pol) to indicate the TM mode, and Y-polarization (Y-pol) to indicate the TE mode.

Here is a simple derivation for the form birefringence. As shown in Figure 3-2, the subwavelength grating is composed of alternating strips of high index medium and low index medium, whose dielectric constants are ε_h and ε_l, respectively. δ is the strip width of the high index medium. Λ is the grating period. The light is incident from the left to the right, whose wave vector **k** is along the *z*-axis. The electric field **E** has *x*-direction and *y*-direction components.

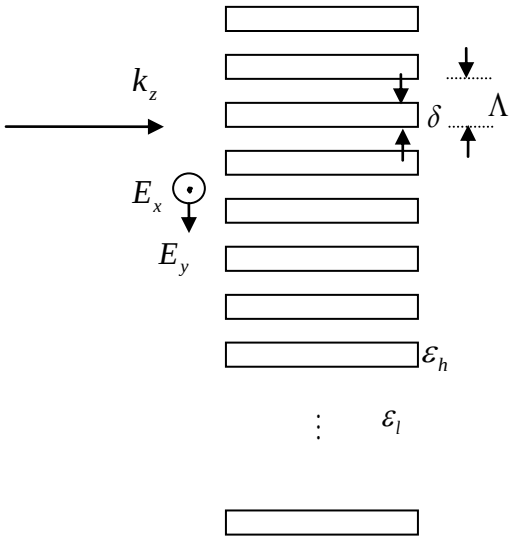

Figure 3-2 Structure of the subwavelength grating.

If the grating period $\Lambda << \lambda$, we can treat any incident wave as a plane wave. Along the *x*-direction, the **E**-field is continuous; hence we have the average displacement along this direction:

$$\begin{aligned} \bar{D}_x &= [\delta\varepsilon_{hx}E_x + (\Lambda-\delta)\varepsilon_{lx}E_x]/\Lambda \\ &= [\alpha\varepsilon_{hx} + (1-\alpha)\varepsilon_{lx}]E_x \end{aligned} \tag{3.1}$$

where $\alpha = \delta/\Lambda$ is the grating duty cycle.

Along the *y*-direction, the displacement is continuous, hence we have the average **E**-field along this direction:

$$\begin{aligned} \bar{E}_y &= [\delta D_y/\varepsilon_{hy} + (\Lambda-\delta)D_y/\varepsilon_{ly}]/\Lambda \\ &= [\alpha/\varepsilon_{hy} + (1-\alpha)/\varepsilon_{ly}]D_y \end{aligned} \tag{3.2}$$

Therefore, we find the 0^{th} order approximation as:

$$\varepsilon_x = \alpha\varepsilon_{hx} + (1-\alpha)\varepsilon_{lx} \tag{3.3}$$

and

$$1/\varepsilon_y = \alpha/\varepsilon_{hy} + (1-\alpha)/\varepsilon_{ly} \tag{3.4}$$

or

$$\varepsilon_y = \varepsilon_{hy}\varepsilon_{ly}/[\alpha\varepsilon_{ly} + (1-\alpha)\varepsilon_{hy}] \tag{3.5}$$

This will introduce a form birefringence with:

$$\begin{aligned} \Delta\varepsilon &= \varepsilon_x - \varepsilon_y \\ &= \frac{[\alpha\varepsilon_{hx} + (1-\alpha)\varepsilon_{lx}][\alpha\varepsilon_{ly} + (1-\alpha)\varepsilon_{hy}] - \varepsilon_{hy}\varepsilon_{ly}}{\alpha\varepsilon_{ly} + (1-\alpha)\varepsilon_{hy}} \\ &\neq \frac{f(1-f)(\varepsilon_h - \varepsilon_l)^2}{f\varepsilon_l + (1-f)\varepsilon_h} \end{aligned} \tag{3.6}$$

Letting $\frac{\partial \Delta\varepsilon}{\partial f} = 0$, we find

$$\Delta\varepsilon_{\max} = \sqrt{\varepsilon_h \varepsilon_l}\left(\sqrt{\frac{\varepsilon_h}{\varepsilon_l}} - 1\right)\left(1 - \sqrt{\frac{\varepsilon_l}{\varepsilon_h}}\right) \tag{3.7}$$

if

$$f_{opt} = \frac{\varepsilon_h - \sqrt{\varepsilon_h \varepsilon_l}}{\varepsilon_h - \varepsilon_l} = \frac{n_h}{n_h + n_l} \tag{3.8}$$

or

$$1 - f_{opt} = \frac{\sqrt{\varepsilon_h \varepsilon_l} - \varepsilon_l}{\varepsilon_h - \varepsilon_l} \tag{3.9}$$

Therefore, if we want to make $\Delta\varepsilon_{\max}$ as large as possible, we need to

(1) enlarge the ratio between ε_h and ε_l;

(2) enlarge the product of ε_h and ε_l;

(3) choose f as f_{opt}.

In the real device design, it is not necessary to utilize the largest index difference $\Delta\varepsilon_{\max}$ always, but this analytical formula provides a guideline for the maximum form birefringence effect that we can possibly achieve.

The effective refractive indices for the TM and TE polarized waves can be written as:

$$\begin{aligned} N_{TM} &= \left[n_{h-TM}^2 \alpha + n_{l-TM}^2 \left(1-\alpha\right) \right]^{1/2} \\ N_{TE} &= \left[\left(1/n_{h-TE}^2\right)\alpha + \left(1/n_{l-TE}^2\right)\left(1-\alpha\right) \right]^{-1/2} \end{aligned} \tag{3.10}$$

where α is the grating duty cycle, i.e., the ratio of the width of a high effective index strip to the period of the grating.

If $\Lambda/\lambda > 1/10$, Eq. (3.10) loses accuracy, but such form birefringence still exists as verified by experiments [59] and the finite-difference time-domain (FDTD) simulations [60], [61]. As an example, Figure 3-3 (a) is a subwavelength grating wedge, and the FDTD-simulated field patterns are shown with a plane wave incident on it and deflected to different angles for (b) the TM and (c) the TE polarizations. The top angle of the wedge is 30 degrees. The high and low strip widths of the wedge are 300 nm and 75 nm, respectively. The refractive indices of the background are 3.147 for TM wave and 3.273 for TE wave. The refractive indices of the high strip are 3.447 for TM wave and 3.452 for TE wave. The refractive indices of the low strip are 1.062 for TM wave and 1.589 for TE wave. These parameters and indices are chosen to be consistent with our PBS design. We can see clearly that the incident TM and TE plane waves are deflected into different directions by this wedge, demonstrating the different effective refractive indices for TM and TE waves induced by the form birefringence.

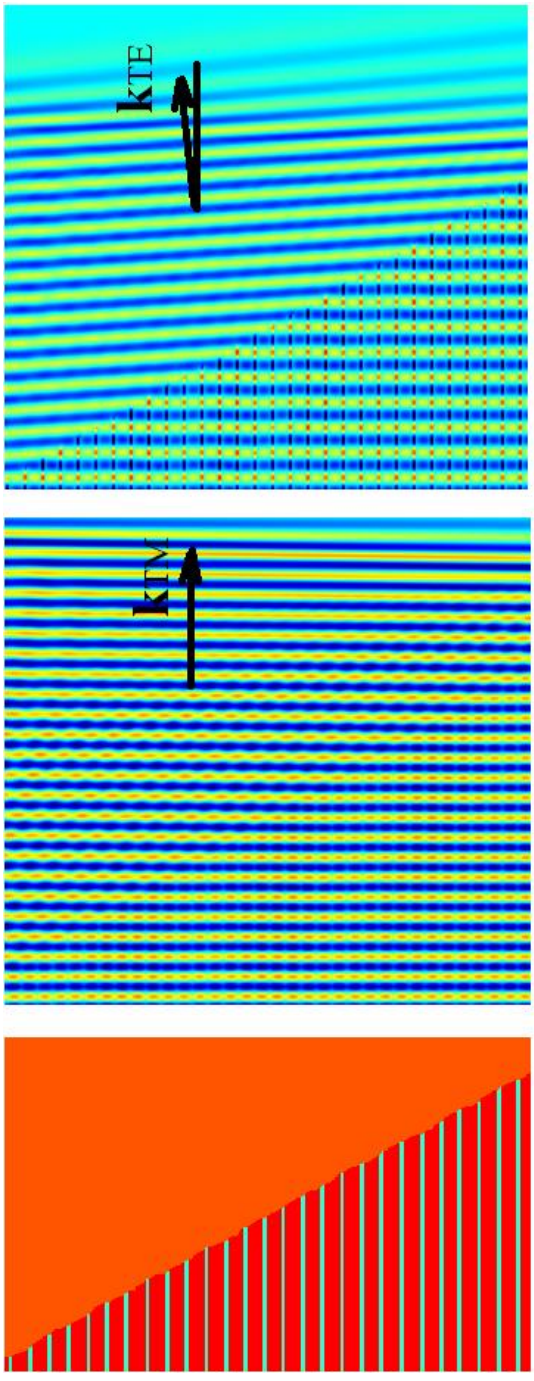

Figure 3-3 (a) The subwavelength grating wedge. (b) The TM and (c) the TE field distributions for a plane wave incident on the wedge. The high and low strip widths of the wedge are 300 nm and 75 nm, respectively.

3.2.3 Diffractive Optics

We can design the preliminary layout structure by the diffractive optics-based analysis in the *y-z* plane. As depicted in Figure 3-1, the incoming light with both polarizations is coupled to the input ridge waveguide, with the guided mode profile $f_m(y)$. The light beam then expands into the *y-z* plane to the first lens in area B, and is collimated to a wide plane wave like beam at the exit. For an ideal system, lenses act as a space Fourier transformer. Thus, after the first lens, the field profile $f_{L1}(y)$ is the Fourier transform of $f_m(y)$. The TM- and TE-collimated beams are further deflected by the wedge to different directions. The field profile after the wedge, $f_w(y)$, is obtained by multiplying $f_{L1}(y)$ with a linear phase shift $p(y)$ along the *y* axis

$$\begin{aligned} f_w(y) &= f_{L1}(y)\exp\left[-jp(y)\right] \\ &= F\left[f_m(y)\right]\exp\left[-j2\pi C(pol)\,y\right] \end{aligned} \tag{3.11}$$

where F[·] indicates the Fourier transform, and $C(pol)$ is a polarization dependent coefficient approximated by

$$C(TM/TE) = (n_0 - N_{TM/TE})\cdot \tan\theta_w / \lambda, \quad \text{for TM/TE mode} \tag{3.12}$$

Here n_0 is the effective index of the platform, and θ_w is the top angle of the wedge. The TM and TE waves are then refocused by the second lens to different positions along the *y* axis. At this focal line, the field profile $f_{L2}(y)$ is the inverse FT of $f_w(y)$

$$\begin{aligned} f_{L2}(y) &= F^{-1}\left\{F\left[f_m(y)\right]\exp\left[-j2\pi C(pol)\,y\right]\right\} \\ &= f_m\left[y + C(pol)\right] \end{aligned} \tag{3.13}$$

where $F^{-1}[\cdot]$ indicates the inverse Fourier transform. Finally, the output waveguides collect the polarized beams at separate locations.

To sum up for this section, this planar PBS design can be realized by different material systems, and is compatible with other slab waveguide based optical components. The device only involves phase changes at the wave front; hence it inherently has a low insertion loss.

3.3 Design Procedure

We choose SOI as the material platform, i.e., crystalline silicon as the substrate, fused silica as the cladding, and amorphous silicon as the guiding layer. If desired, our PBS design can be implemented on other material systems. The effect of the intrinsic material anisotropy of the silicon guiding layer is not considered.

3.3.1 Material Indices

We adopt the Si and SiO_2 material indices in [62]-[64]. The dispersion curve of amorphous Si is shown in Figure 3-4. The material indices of Si and SiO_2 in the optical band of 1.5 μm to 1.6 μm are shown in Table 3-3.

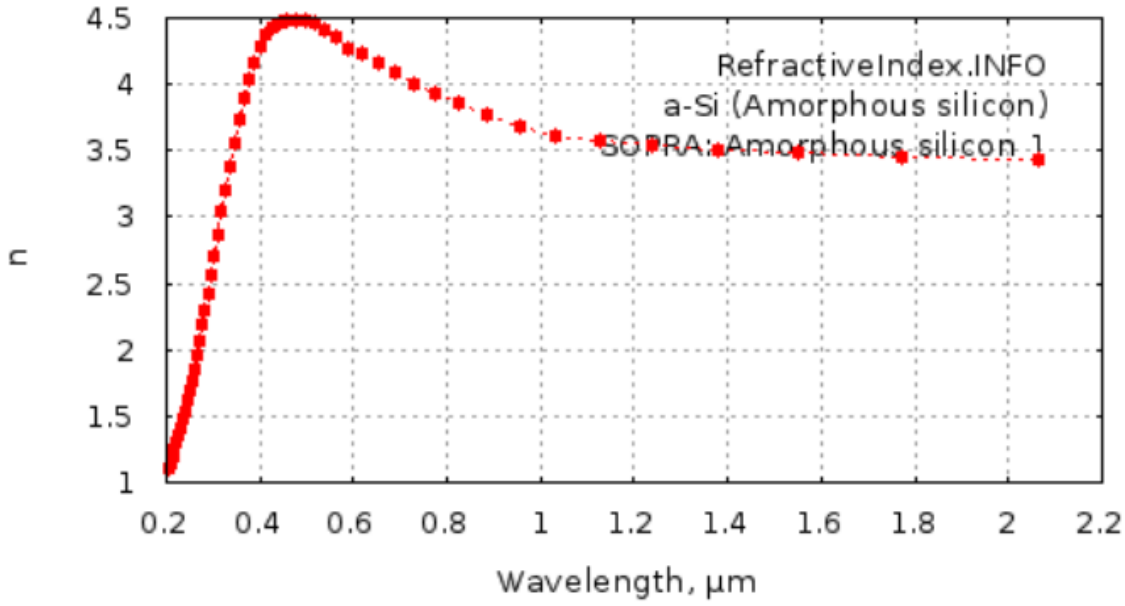

Figure 3-4 The refractive index of amorphous Si [64].

Table 3-3 Material indices of Si and SiO_2 in the optical band of 1.5 µm to 1.6 µm.

λ(µm)	n(SiO_2)	n(Si)
1.5	1.445	3.486
1.525	1.444	3.483
1.55	1.444	3.480
1.575	1.444	3.477
1.6	1.443	3.473

3.3.2 Effective Indices

The SOI slab waveguide structure is shown in Figure 3-5. We use the transfer-matrix method (TMM) to calculate the TE and TM mode profiles and effective indices for the SOI slab waveguide [65], [66].

Figure 3-6 shows the mode profiles for the SOI slab waveguide with cladding layer thickness of 0.5 μm, guiding layer thickness of 0.5 μm, at the wavelength of 1.55 μm. (a) is the mode profile for TM mode, and (b) is for TE mode.

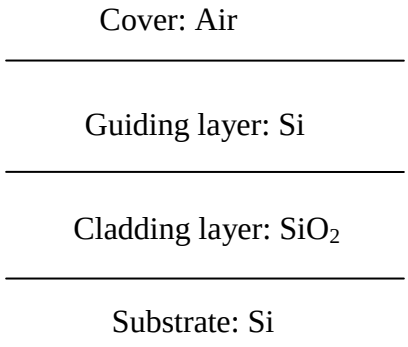

Figure 3-5 Slab waveguide structure of SOI.

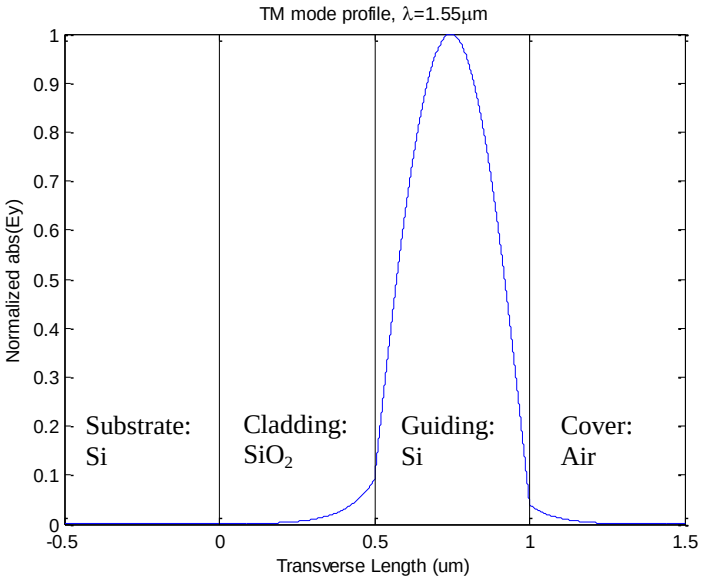

(a)

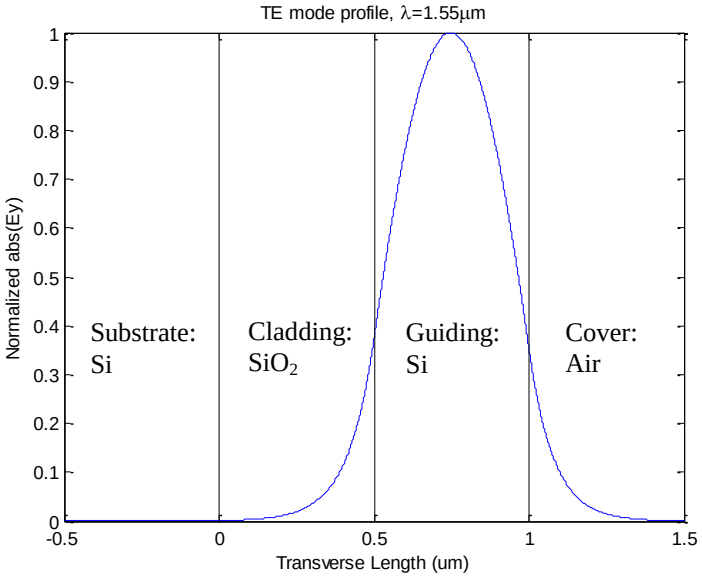

(b)

Figure 3-6 Mode profile for a SOI slab waveguide with cladding layer thickness of 0.5 μm, guiding layer thickness of 0.5 μm, at the wavelength of 1.55 μm. (a) TM mode. (b) TE mode.

As can be seen from Figure 3-6, the majority of the mode profile is concentrated in the Si guiding layer, and the intensity of the mode quickly decays in the cladding and cover layers. Therefore, the guiding layer thickness controls the effective mode index. We then study the effective indices of the fundamental TM and TE mode as a function of the Si guiding layer thickness, as shown in Figure 3-7. The difference of the effective indices between the TM and TE mode is shown in Figure 3-8.

For the etched area in the wedge, shown as area C low in Figure 3-1, the Si guiding layer is very thin or does not even exist. Therefore, no guided mode is supported in this area. We can obtain its approximate effective index by calculating the mode profile in the background, i.e. area D in Figure 3-1, weighted by the index profile in the etched low index area of the wedge.

For TE mode,

$$n_{eff}^2 = \frac{\int n(x)^2 E_y(x)\,dx}{\int E_y(x)\,dx} \tag{3.14}$$

For TM mode,

$$n_{eff}^2 = \frac{\int H_y(x)\,dx}{\int \frac{H_y(x)}{n(x)^2}\,dx} \tag{3.15}$$

where E_y and H_y are the mode profiles in the background for TE and TM, respectively; $n(x)$ is the index profile for the etched low index area of the wedge.

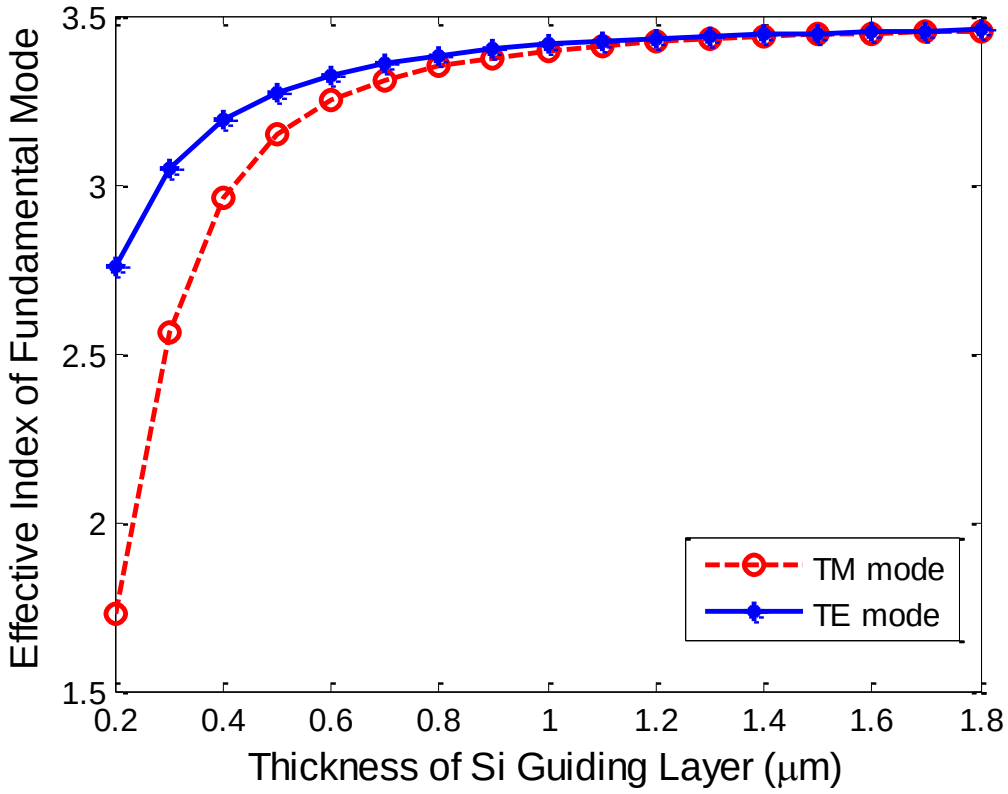

Figure 3-7 Effective TM and TE mode indices of SOI slab waveguide as a function of Si guiding layer thickness.

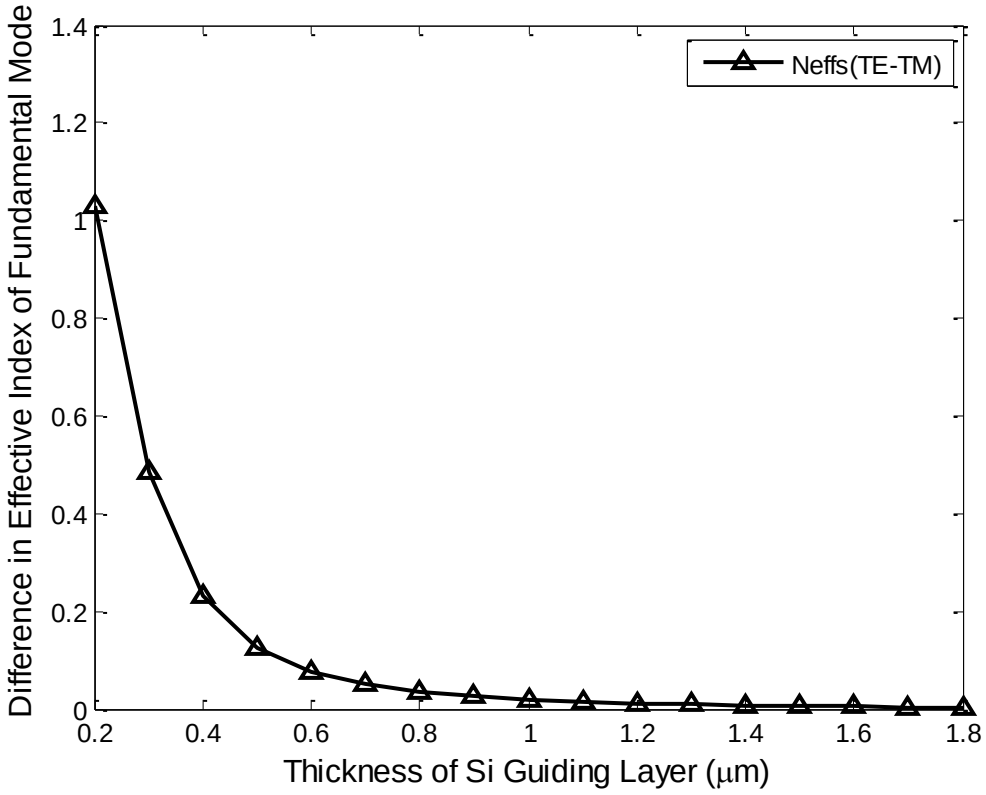

Figure 3-8 Difference of the effective TM and TE mode indices of SOI slab waveguide as a function of Si guiding layer thickness.

Using Si guiding layer with a thickness of 0.5 μm as the background, we can calculate the effective index of the etched low index wedge area as a function of the etching depth from the background, shown in Figure 3-9, at the wavelength of 1.55 μm.

Two factors must be considered when choosing the proper thickness of the Si guiding layer for different areas in the PBS: 1) Different areas must have enough difference in the effective refractive indices, so that each area can manipulate light wave effectively as a functional block. Thus, the Si guiding layer in each area would require a different thickness. 2) For TM and TE wave, the different behavior should come from the wedge of the form birefringence. For the other parts of the PBS, the difference in the refractive indices for TM and TE waves should not be too large, since the other parts are supposed to function the same for TM and TE waves, and we want a similar PBS performance for TM and TE waves.

Therefore, the thickness of each layer for different areas is designed as: the cladding layer 0.5 μm; the guiding layer 0.52 μm for area A, 1.6 μm for B and C high, 0.1 μm for C low, and 0.5 μm for D.

To sum up for the effective index calculation: Using TMM, we can extract the effective refractive indices of the corresponding slab waveguide in the vertical direction for different areas in Figure 3-1. We then calculate the effective indices in the wedge grating area using Eq. (3.10) for the TM and TE waves, respectively. Those effective indices obtained are listed in Table 3-4 for the wavelength of 1.55 μm.

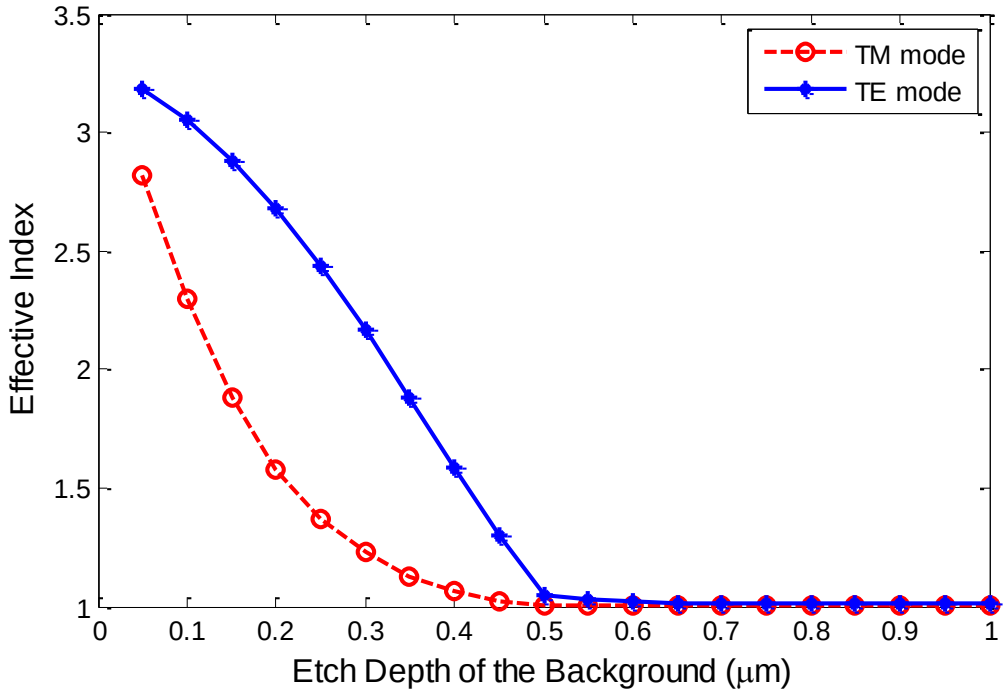

Figure 3-9 The effective index of the etched low index wedge area as a function of the etching depth from the background, at the wavelength of 1.55 μm.

Table 3-4 Device structure parameters at 1.55 μm

	TM (X-pol)	TE (Y-pol)
Platform effective refr. index n_0	3.147	3.273
Waveguide effective refr. index	3.172	3.285
Lens effective refr. index	3.447	3.452
High strips of wedge effective refr. index n_h	3.447	3.452
Low strips of wedge effective refr. index n_l	1.062	1.589
Duty cycle of wedge grating α	0.8	
Wedge effective refr. index N	3.119	2.614
Wedge top angle θ_w (degrees)	30	
Lens aperture (μm)	50	
Lens major radius to minor radius ratio	3.14	
Lens 1 (collimating) focal length (μm)	115.0	
Lens 2 (refocusing) focal length L_{f2} (μm)	80.5	156.5
Lens 2 major axis rotate angle[a] (degrees)	4.0	
Output beam deflecting angle[a] (degrees)	0.8	6.0
Input waveguide width (μm)	3.8	
Output waveguide width (μm)	1.8	3.8
Device width (μm)	80	
Device length (μm)	300	

Note that refr. stands for refractive.
[a]Angles are measured with respect to *z*-axis.

3.3.3 Lens Design

The lenses' shapes are derived to be elliptical [57]. A schematic diagram of a lens structure with an aperture *D* is shown in Figure 3-10.

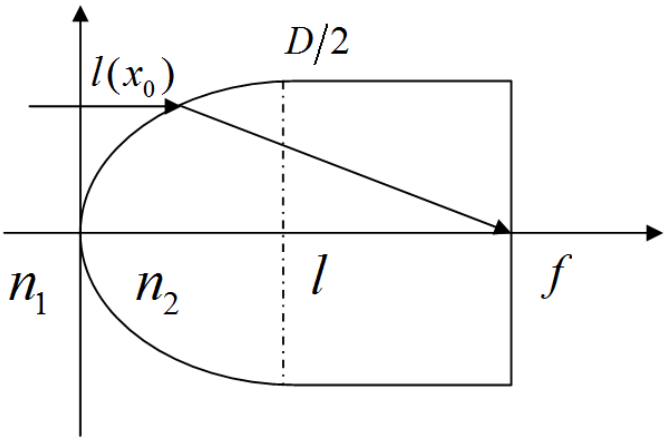

Figure 3-10 Schematic diagram of a lens structure.

The refractive indices inside and outside the lens structure are denoted by n_2 and n_1, respectively. According to the ray optics theory [67], the lens should be shaped in such a way that the collimated light coming from the left to the right is focused at the point *f* or vice versa, i.e. optical paths of the rays in the collimated beam should be all equal. This is shown in Eq. (3.16).

$$n_2 f = n_1 l(x_0) + n_2 \sqrt{[f - l(x_0)]^2 + x_0^2} \tag{3.16}$$

This can be rewritten in the following form

$$\frac{[l(x_0)-a]^2}{a^2}+\frac{x_0^2}{b^2}=1 \tag{3.17}$$

where

$$a=\frac{n_2 f}{n_1+n_2}$$
$$b=f\sqrt{\frac{n_2-n_1}{n_1+n_2}} \tag{3.18}$$

We can see that the lens takes an elliptical shape with a as the long axis and b as the short axis. This provides a guideline to our lens design, while the parameters need to be adjusted with the field distribution calculated by BPM.

The TM and TE beams have different effective indices throughout the device; therefore the focal length of the second lens needs to be adjusted separately for each polarization. Since the focal length for the TE wave is larger, we design the second lens according to the TE wave, cut out the excess part from the TM focal line, and place the output waveguide for the TM wave. Increasing the distance between the two lenses will slightly degrade the performance of the PBS, and also unnecessarily enlarge its length. We choose this distance to be 24 μm in order to fit in the wedge.

3.3.4 Wedge and Waveguide Design

For the wedge, a proper beam splitting angle must be obtained by controlling n_l, α and θ_w. If the splitting angle is too small, a large portion of the TM and TE beam profiles are overlapped, and therefore the crosstalk and insertion loss are high. If the splitting angle is too big, it requires further etching down of the layers to get a small n_l, and the

scattering loss for the TE wave is high since its deflected angle is large. The grating duty cycle α was chosen to be slightly offset from the value generating the largest index difference between the two polarizations in order to make the deflected angle and thus, loss of the TE wave, smaller.

The widths of the input and output waveguides are designed to minimize the insertion loss and crosstalk. The input waveguide width is 3.8 μm, and supports 2 modes for both TM and TE polarizations. For the output waveguide, the TE output port is 3.8 μm in width, where 2 modes can exist. In this way, more lightwave can be collected for TE mode, so that the insertion loss of the device can be reduced. The waveguide of TM output port is 1.8 μm in width, supporting only 1 mode. As can be seen in the field distribution in Figure 3-12 (b), the TM polarization is well re-focused by the second lens into a narrow profile, thus the output waveguide of a small width can guarantee a small insertion loss for TM mode, and a small crosstalk at the same time.

With all the considerations in mind, the structure is designed with its parameters summarized in Table 3-4 for the operating wavelength of 1.55 μm.

3.4 Simulation

3.4.1 Simulation Setup of 2-D Beam Propagation Method (BPM)

We use the wide-angle 2-D beam propagation method (BPM) with eight perfectly matched layers (PMLs) [68] to numerically simulate the field distribution. The structure setup for 2-D BPM is shown in Figure 3-11.

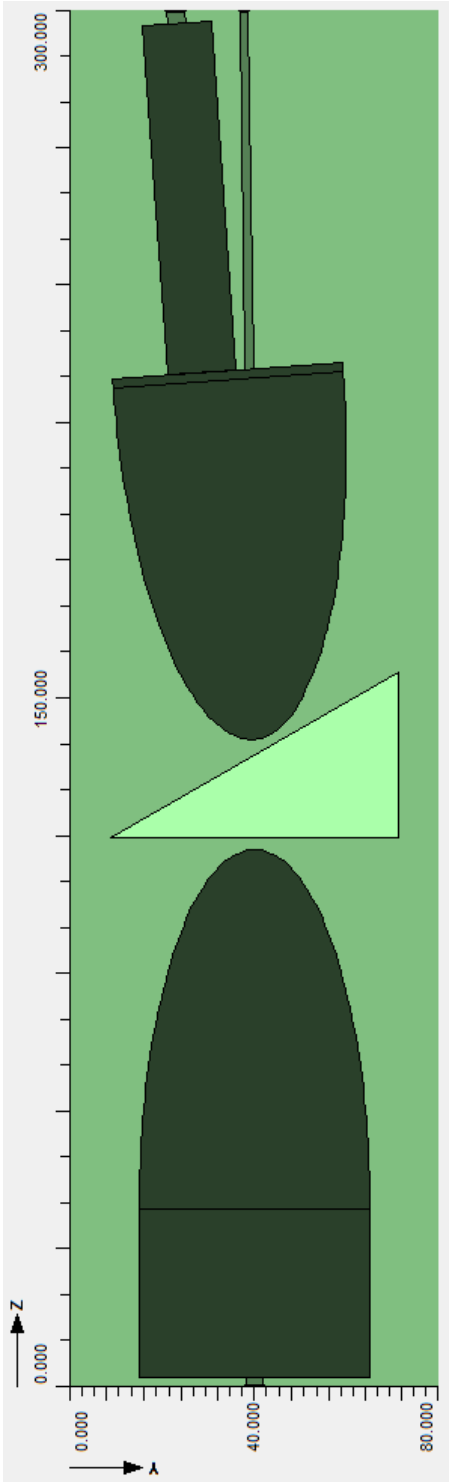

Figure 3-11 The 2-D structure of the polarization splitter.

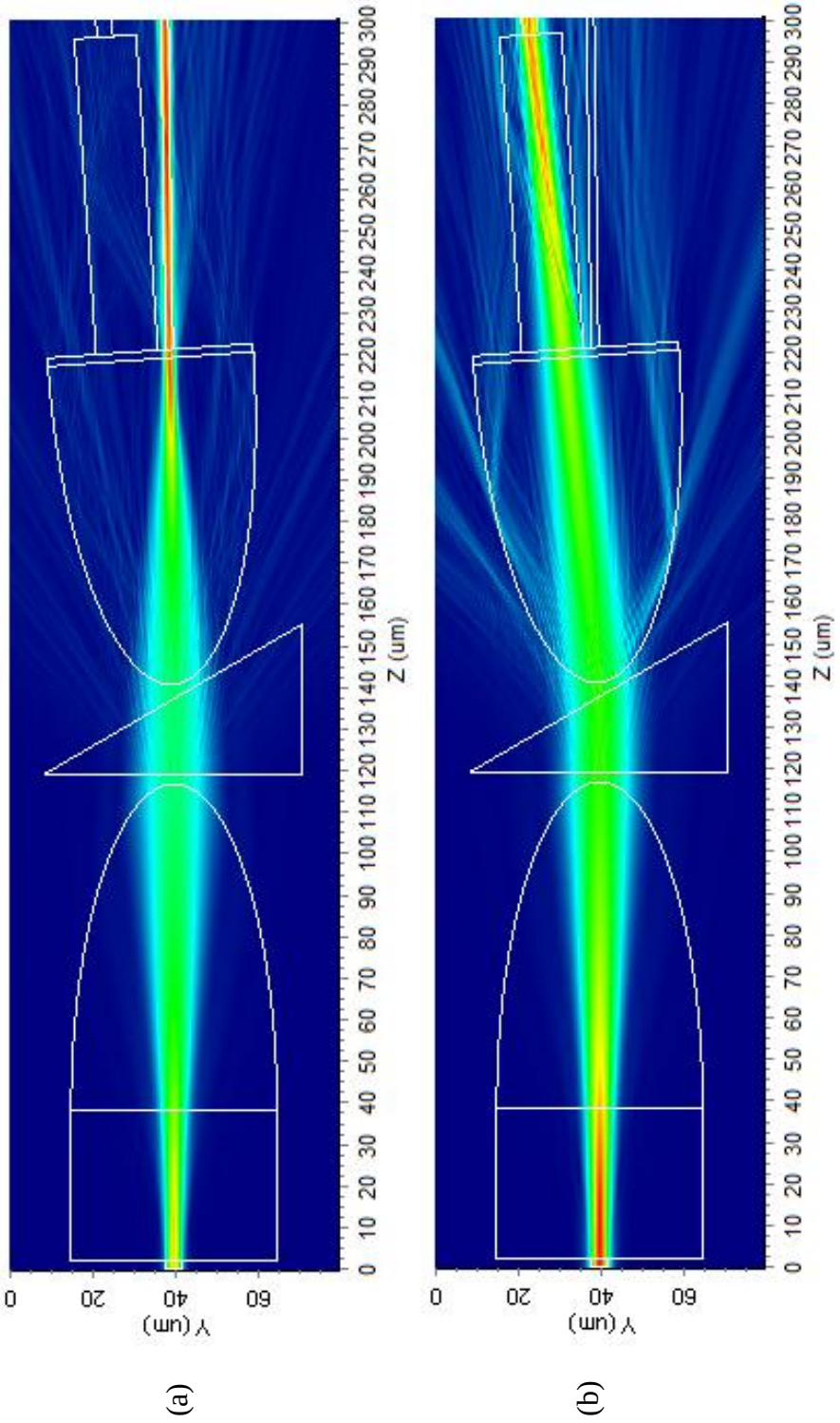

Figure 3-12 Top view field distribution by 2-D BPM simulation for (a) the TM and (b) TE polarizations at 1.55 μm.

The BPM algorithm here does not need to deal with large index variations, since we adopted low effective-index contrast in the design for low reflection and scattering. The scheme factor is set to 0.5, and the wide-angle Pade order is 2.

Since we adopted low effective-index contrast, the loss due to the Fresnel reflection on the interfaces is not very significant. Assume that the reflective indices of two medium are n_1 and n_2, respectively. The loss due to the interface reflection between these two medium can be roughly estimated by the power reflectivity for normal incidence using $[(n_1-n_2)/(n_1+n_2)]^2$, since the deflected angle is 6 degrees or less in our PBS. By cascading the interface reflection throughout the device, this loss is calculated to be 0.033 dB for TM and 0.121 dB for TE. Therefore, we did not count in the Fresnel reflection loss.

3.4.2 Simulation Results at the Wavelength of 1.55 μm

The corresponding fields (top view) for the TM and TE polarizations are shown in Figure 3-12 (a) and (b), respectively, at the wavelength of 1.55 μm.

The insertion loss and crosstalk are calculated from the optical powers measured at the input and output ports. At the input port, the fundamental mode is launched. For TM output port, only one mode is supported. For the TE output port, two modes are supported.

The insertion loss can be calculated as the ratio of the output power to input power for TM and TE modes, respectively, as shown below

$$IL = -10\log_{10}\left(\frac{P_{out}}{P_{in}}\right) = -10\log_{10}\left(\frac{\sum_{\text{modes}} |A_{out}|^2}{|A_{in}|^2}\right) \tag{3.19}$$

where $|A|$ is the amplitude of modes.

The crosstalk is defined as the ratio of the power measured at the undesired output port to the power measured at the desired output port.

$$CT = 10\log_{10}\left(\frac{P_{undesired}}{P_{desired}}\right) \tag{3.20}$$

For TM mode, we launch TM (X-pol) mode at the input waveguide, and measure the power at the TE output port $P_{X\to TE}$ and the power at the TM output port $P_{X\to TM}$. The crosstalk can be calculated as

$$CT_{X-pol} = 10\log_{10}\left(\frac{P_{X\to TE}}{P_{X\to TM}}\right) = 10\log_{10}\left(\frac{|A_{X\to TE1}|^2 + |A_{X\to TE2}|^2}{|A_{X\to TM}|^2}\right) \tag{3.21}$$

where the subscript $X \to TE1$ denotes that the input is the fundamental TM mode (X-pol), and the output is the fundamental TM mode measured at the TE output port (TE1). The $TE2$ in the subscript denotes that the output is the second order TM mode measured at the TE output port.

For TE mode, we launch TE (Y-pol) mode at the input waveguide, and measure the power at the TM output port $P_{Y\to TM}$ and the power at the TE output port $P_{Y\to TE}$. Similarly, the crosstalk can be calculated as

$$CT_{Y-pol} = 10\log_{10}\left(\frac{P_{Y\to TM}}{P_{Y\to TE}}\right) = 10\log_{10}\left(\frac{|A_{Y\to TM}|^2}{|A_{Y\to TE1}|^2 + |A_{Y\to TE2}|^2}\right) \tag{3.22}$$

Table 3-5 Device characteristic parameters

Simulated performance at 1.55 μm	Value (dB)
Insertion loss of the TM polarization	0.283
Insertion loss of the TE polarization	0.595
Crosstalk of the TM polarization	-32.1
Crosstalk of the TE polarization	-32.2

The results at the wavelength of 1.55 μm are summarized in Table 3-5.

3.4.3 Band Performance

The optical band performance of the PBS relies on the material dispersion and waveguide dispersion. Here we summarize the material indices (indicated by n) and effective indices (indicated by N) in Table 3-6. d_Si denotes the thickness of the Si guiding layer.

We calculate the insertion loss and crosstalk in the optical band from 1.5 μm to 1.6 μm, and plot the results in Figure 3-13. We can see that our PBS has a good band performance with insertion loss less than 0.9 dB and crosstalk below -30 dB in this optical band.

Table 3-6 Material indices and effective indices for different areas in the polarization splitter in the optical band of 1.5 μm to 1.6 μm.

λ(μm)	n(SiO_2)	n(Si)	Background (Area D) d_Si = 0.5 μm	Waveguide (Area A) d_Si = 0.52 μm	Lens and Wedge high (Area B) d_Si = 1.6 μm	Wedge low (Area C) d_Si = 0.1 μm	Wedge (α =0.8)
1.5	1.445	3.486	N(TM): 3.175	N(TM): 3.198	N(TM): 3.455	N(TM): 1.061	N(TM): 3.126
			N(TE): 3.290	N(TE): 3.301	N(TE): 3.459	N(TE): 1.589	N(TE): 2.616
1.525	1.444	3.483	N(TM): 3.161	N(TM): 3.185	N(TM): 3.451	N(TM): 1.062	N(TM): 3.123
			N(TE): 3.281	N(TE): 3.293	N(TE): 3.456	N(TE): 1.589	N(TE): 2.615
1.55	1.444	3.480	N(TM): 3.147	N(TM): 3.172	N(TM): 3.447	N(TM): 1.062	N(TM): 3.119
			N(TE): 3.273	N(TE): 3.285	N(TE): 3.452	N(TE): 1.589	N(TE): 2.614
1.575	1.444	3.477	N(TM): 3.133	N(TM): 3.159	N(TM): 3.443	N(TM): 1.063	N(TM): 3.116
			N(TE): 3.265	N(TE): 3.277	N(TE): 3.448	N(TE): 1.590	N(TE): 2.613
1.6	1.443	3.473	N(TM): 3.118	N(TM): 3.145	N(TM): 3.438	N(TM): 1.063	N(TM): 3.112
			N(TE): 3.255	N(TE): 3.268	N(TE): 3.443	N(TE): 1.590	N(TE): 2.612

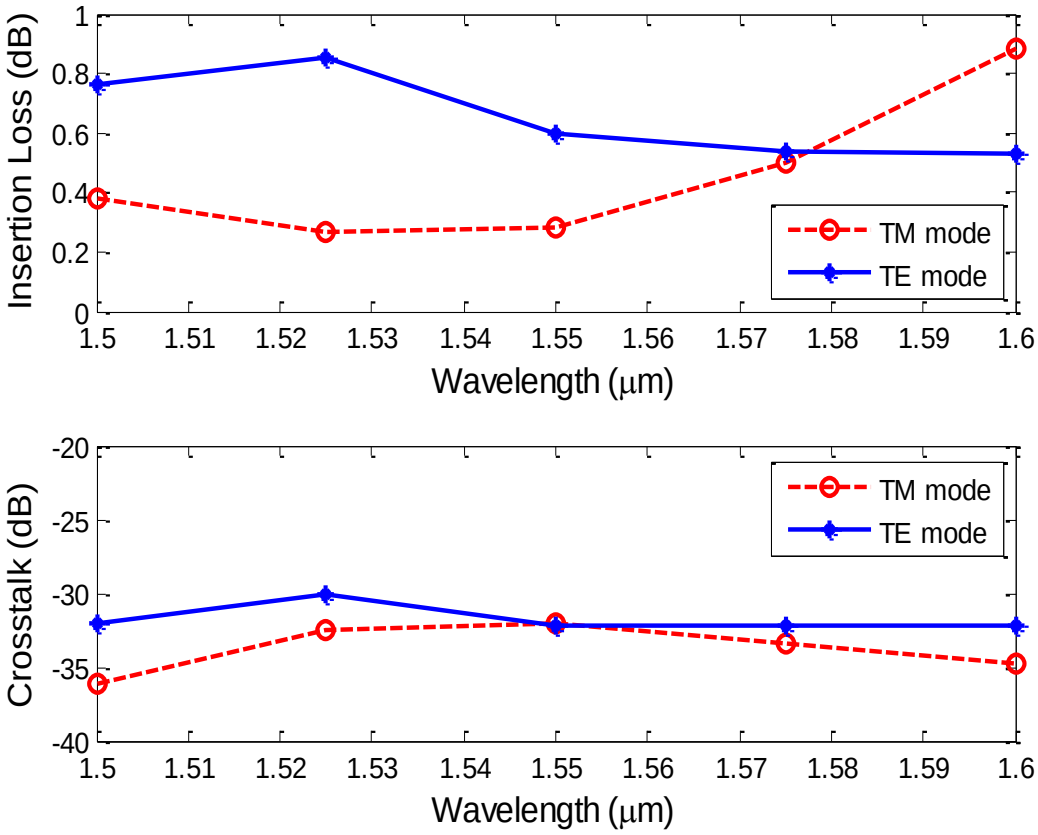

Figure 3-13 Insertion loss and crosstalk of the PBS in the band 1.5 μm - 1.6 μm.

The most sensitive thickness of the guiding silicon layer in this PBS design is that of area A, the input and output waveguides. At the operating wavelength of 1.55 μm, a (+/-) 10 nm variation of the guiding layer thickness will only increase the insertion loss by less than 0.17 dB, and the crosstalk remains below -30 dB. This submicron etching accuracy on SOI can be achieved by using the inductively coupled plasma reactive ion etching (ICP-RIE) with proper gas chemicals [69].

3.5 Summary

We have designed and numerically simulated a newly proposed PBS device based on a planar waveguide platform. A wedge made of a subwavelength grating utilizes the form birefringence to enlarge the effective refractive index difference between the TM and TE polarizations, and splits the two polarization beams to different directions. The insertion loss is less than 0.9 dB for the designed operating wavelength band of 1.5 μm to 1.6 μm. The crosstalk between the two polarizations is below -30 dB. The whole device size is 300 μm × 80 μm, and can potentially be further reduced by improving the lens design. This PBS device can be readily fabricated by lithography and etching, and can be monolithically integrated with other optical components on the same platform. This design can also be extended to other material systems and other wavelength bands to meet the required specifications.

Chapter 4.

Investigation of Mode Partition Noise in Fabry-Perot Laser Diode

4.1 Introduction

As stated in the earlier chapters, the passive optical network (PON) is a cost-efficient solution to the last-mile bottleneck in optical communication networks. And to further reduce the cost per subscriber, a Fabry-Perot (FP) laser diode (LD) is preferred as the transmitter at the optical network units (ONUs) because of its lower cost compared to distributed feedback (DFB) LD. However, the mode partition noise (MPN) associated with the multi-longitudinal-mode FP-LD becomes the limiting factor in the network.

Here we review the previous works on the study of MPN, including the theoretical analysis, experimental measurements, and suppression schemes of MPN.

The instantaneous power of each longitudinal mode in the laser diode fluctuates even though the total power of laser diode remains relatively constant. This is caused by the mode competition in the laser cavity where various modes compete for a common injected carrier population. This phenomenon is called the mode partition noise (MPN). In the absence of fiber dispersion, MPN would be negligible as all the modes propagate synchronously. However, when chromatic dispersion is present, different modes travel at

slightly different speeds along the fiber, leading to the distortions at the decision instant. MPN can even cause the bit error rate (BER) floor, where the system performance will not improve even though the received power increases. In this case, MPN becomes the dominant limiting factor in an optical transmission system. Therefore, it is necessary to pay more attention to the effects of MPN in laser transmission systems, especially for 2.5 Gbit/s and 10 Gbit/s high-speed transmission application with multi-mode FP-LD, because the fiber dispersion penalty will be significantly enhanced when MPN is remarkable.

A simple mathematical model of MPN was derived by Okano et al. in 1980 [70], in which the Q-factor and power penalty caused by MPN were formulated, and infinite power penalty was presented. However, in the derivation of MPN model, the joint probability distribution of the powers of various longitudinal modes was assumed known, while in practice it is hard to obtain the knowledge of the probability characteristic of laser modes. A more general and practical model of MPN was proposed by Ogawa in 1982 [71], [72], and MPN was evaluated by calculating or measuring the mode partition coefficient, k-factor, that indicates the degree of mode fluctuation. This method avoids using the knowledge of probability distribution of longitudinal modes, and the critical assumption of this model is that all the modes are contributed by stimulated emission only. A close-form of variance of MPN was also presented by supposing the use of cosine waveform for each longitudinal mode [71]. The mode-resolved distributions were shown both for the main mode and the side modes by Ogawa in 1984 [73], and the probability of the side modes to carry a significant portion of the total optical power was

studied. In Ogawa's works, the statistics of longitudinal mode powers were considered only within the symbol duration. Campbell studied the correlations between the mode powers for different symbol periods [74], and he further completed the mathematical model of MPN.

D. Marcuse developed the numerical simulation method of solving the Langevin noise driven rate equations for a single-cavity laser diode, and presented the probability distribution of each longitudinal mode obtained from photon counting statistics in 1984 [75], [76]. Marcuse showed that the photon probability distribution narrows with increasing gain saturation parameter, decreasing cavity distributed loss, increasing bias current, increasing output power, and decreasing laser length. Besides, if two modes are symmetrically located at either side of the gain peak, they will compete for optical power, resulting in a wide flat photon probability distribution for these two modes. Thus, decreasing the gain peak offset from the central longitudinal mode can narrow the photon probability distribution. It was also noticed that when the injection current is modulated with pulses, multi-modes will be present at the turn-on transient, and the central mode may carry less power than one of its neighboring mode if the pulse is very short. Nguyen followed this approach, and used a noise-driven 21-mode rate equation laser model for simulations [77]. He showed that increasing the gain compression factor, also noted as self-saturation, can suppress MPN, and the central modes would have Gaussian probability distribution regardless of the material gain peak offset from the cavity modes. He also showed that asymmetric nonlinear gain alters the mode distributions, but its effect on MPN is weaker than that of the self-saturation.

In the past ten years, several groups have investigated on the mode hopping (or switching) dynamics for semiconductor lasers. M. Ahmed and M. Yamada performed extensive simulations of noise-driven multi-mode rate equations, and classified the laser operation into four regimes, i.e. stable single mode, jittering single mode, stable multi-mode, and hopping multi-mode [78]. They found that the laser operation regime depends on the injection current and the linewidth enhancement factor (α). When the injection current is slightly above the threshold current, the laser operates in the stable multi-mode regime. If both the injection current and the α-factor are large, the laser will most likely to operate in the hopping multi-mode regime. This regime is featured with periodic rotation of four lasing modes even without laser Langevin noise, with a repeating frequency in the 10 megahertz range. The lasing mode follows the switching sequence from the blue to red, and then restarts from the bluest mode. The Langevin noise causes the instant power fluctuations, and slightly modulated the rotation frequency. And the Langevin noise can also stimulate the mode rotation even when the deterministic simulation shows stable multi-mode operation, as shown for the case of an InGaAsP laser with α-factor of 4 and injection current twice the threshold. Time-dependent experiment measurements proved this periodic multi-mode switching behavior [79]-[81]. The origin of this periodic mode switching is the large spectral asymmetry in the cross-saturation coefficient due to the asymmetric material gain spectrum. This asymmetry can be induced by a large linewidth enhancement factor, and/or a large differential material gain coefficient [78]-[81]. The quantum-well lasers are more prone to this mode switching dynamics than the bulk lasers [81].

With the increasing demand for data rate in fiber-optic communications, the effect of fiber dispersion on the performance of lightwave systems using multimode semiconductor laser becomes a challenging issue for long-distance transmission in optical communications. The presence of MPN in laser transmission systems with dispersive fibers leads to remarkable performance degradation. Many important researches have been carried out in the past thirty years to study the interaction of MPN with fiber dispersion. G. P. Agrawal investigated the dispersion penalty for a 1300-nm lightwave system with multimode semiconductor laser [82], and presented a more general expression of variance of MPN based on cosine waveforms as compared to that given by Ogawa in [71]. In his study, the acceptable range of wavelength deviation to the zero-dispersion wavelength was calculated for different values of k. He also stated that the numerical value of k is relatively uncertain and depends on many parameters such as bit rate, modulation depth and the spectral width. So, he assigned the typical k values in the range of 0.5 to 1.0, as suggested by the experimental measurements in his calculations of MPN. MPN-induced impairments were extensively studied in different ways. Cheung et al. developed an empirical formula that relates the bit rate and distance for a dispersion-limited system when MPN was considered, in which the multimode InAsGaP/InP laser was operating at 1500 nm [83]. Wentworth et al. presented theoretical expressions for the MPN spectra for the light from a nearly single-mode or strongly multimode semiconductor laser after passing through a length of dispersive fiber [84]. The relationship between the mode partition constants presented by Okano [70] and laser diode characteristic was clarified using rate equations by Iwashita and Nakagawa [85].

They showed that the mode partition noise is independent of the wavelength and the structure of the Fabry-Perot type laser diodes. MPN is also studied for single-mode lasers. Shen and Agrawal analyzed the mode partition noise in single-frequency semiconductor lasers by relating the variance of MPN with mode suppression ratio (MSR), and they claimed that MPN in single-frequency lasers may not be an issue when a large MSR is achievable (> 1000) [86]. It was also demonstrated by Lathi et al. that suppressing the side modes can reduce both MPN and the total noise [87]. The effect of MPN is also determined by the number of longitudinal modes, which was studied by Wang and Chan [88]. They presented that to achieve error-free transmission at 1 Gbit/s with free-running gain-switched FP laser, a sufficiently large number of modes should be generated. In their work, at least 9 modes in laser can guarantee the error-free performance.

Among those studies, J. C. Cartledge did a complete research on MPN and its performance implications in the link using both statistical formula model and rate equation simulations for directly modulated nearly-single-longitudinal-mode lasers [89]-[91]. He demonstrated that the floor in the probability of error curve for MPN is dependent upon a variety of laser and link parameters, as summarized below:

a) Laser parameters.
   - Threshold gain difference between the lasing mode and the dominant side mode.
   - Gain compression factor.
   - Spontaneous emission coefficient.
   - Mode wavelength separation, i.e. mode spacing.

b) Modulation characteristics.
   - Laser bias current and modulation current pulse shape.
   - Encoding format, i.e. non-return-to-zero (NRZ) and return-to-zero (RZ).
   - Bit pattern, particularly for the NRZ.
   - Bit rate.

c) Fiber dispersion and length.

d) Clock recovery in the receiver, i.e. sampling time.

We can see that a) and b) relate to the transmitter, where a) is the intrinsic laser parameter, and b) is the operating condition. c) is the fiber characteristic, and d) is at the receiver end. Thus, the MPN impact in a network really depends on the whole link.

In addition, MPN in wavelength-division multiplexing (WDM) systems was investigated. Clarke analyzed the MPN caused by the sharp cut-off optical filters employed in demultiplexers, and presented that low-power modes made significant contribution to MPN [92]. Another work on MPN in WDM systems by Anandarajah et al. was focused on the cross-channel interference introduced by MPN. In a 2-channel WDM system spaced by 10 nm, the cross-channel interference was observed and the system performance was degraded when the side mode suppression ratio of one of the sources decreased [93]. The MPN in fiber lasers was also experimentally demonstrated by Liao and Agrawal [94], and a numerical model was developed using the Langevin rate equations. In one study that discussed the parameters affecting MPN in laser transmission systems, it was shown that BER varies periodically when accumulated dispersion

increases [95]. However, in other works, BER monotonously increases with the accumulated fiber dispersion [96].

There are some literatures discussing about the suppression of MPN using the reflective semiconductor optical amplifier (RSOA). RSOA enables a cost effective transmitter in which the colorless amplification and signal modulation can be implemented simultaneously [97]. This attractive feature makes it a strong candidate for WDM-PON because the use of RSOA avoids the need of tunable laser sources at the customer premises. Another important characteristic of SOA is its gain saturation effect, which has been utilized to reduce the MPN. In a study completed by Sato and Toba, they presented how to use a semiconductor optical amplifier (SOA) to reduce MPN with mode-locked FP-LD [98]. In their work, the relative intensity noise (RIN) of the filtered output from arrayed waveguide grating (AWG) showed an extreme increase of mode partition noise at low frequencies. The SOA acted as a high-pass filter. After passing through SOA, the MPN of the output signal at low frequencies was significantly suppressed. Another implementation of SOA for the reduction of MPN was demonstrated by Kim et al. In their work, simultaneous wired and wireless WDM radio-over-fiber (RoF) transmission using FP-LD was presented, and RSOA was used both for the modulation of certain channel data and for the reduction of MPN [99]. The simplest method to reduce MPN was presented in the study by Mandridis et al. [100]. It was shown that the correlated electrical mode partition noise of periodic electrical signal can be suppressed when the electrical signal is first up-converted to optical domain, and then passes through a photodiode (PD). PD acts as an optical frequency mixer, such that the output of PD is

the mixing of all the neighboring components of the optical spectrum, leading to the cancellation of MPN.

The MPN impact of FP-LD in PON technology has also been explored, as well as using forward error correction (FEC) to effectively mitigate it. Yi et al. studied the MPN in a 1.25 Gb/s burst-mode gigabit passive optical network (GPON), and they showed via simulations and experimental measurements that FEC can provide a 2.7 dB effective optical gain when MPN dominates [27]. Pato et al.'s work in 2007 investigated the impact of MPN on the performance of upstream transmission of 10 Gb/s Ethernet passive optical networks (EPON) with FP-LDs in optical network units (ONU) [101]. They have shown that a 1.5 dB gain from FEC is achieved at the BER of 10^{-12}. The conclusion was made that if commercially available FP-LDs are employed, to enable up to 20 km transmission, one must reduce the source spectral width and fiber dispersion. However, if FEC is applied, the achieved receiver power gain can be translated to less stringent requirement for source spectral width and/or fiber dispersion.

In this chapter, we will investigate the MPN characteristics of FP laser diode using the time-domain simulation of noise-driven multi-mode laser rate equation. The probability density functions are calculated for each mode. The k-factor is a simple yet important measure for the noise power, and it is related with the power penalty of MPN in analytical formulas. However, it is usually a fitted or assumed value in the penalty simulations. In this chapter, the sources of the k-factor are studied with simulation, including the intrinsic source of the laser Langevin noise, and the extrinsic source of the bit pattern.

4.2 Noise-driven Multi-mode Laser Rate Equation

Jensen et al. used a set of multimode rate equations with Langevin noise terms to model the FP laser [102], and we follow their model in our simulation.

$$\frac{dN}{dt} = J - R(N) - \sum_i \Gamma G_i(N) S_i + F_N(t) \tag{4.1}$$

$$\frac{dS_i}{dt} = \left[\Gamma G_i(N) - \frac{1}{\tau_p} \right] S_i + \beta_i B N^2 + F_i(t) \tag{4.2}$$

Here N is the carrier number, S_i is the photon number in the *i*-th longitudinal mode, J is the pump in the unit of electrons/second, $R(N)$ is the total spontaneous recombination rate, Γ is the mode confinement factor, τ_p is the photon lifetime, β_i is the fraction of spontaneous emission coupled into mode *i*, B is the band-to-band recombination coefficient. $F_N(t)$ and $F_i(t)$ are Langevin noise terms.

The gain $G_i(N)$ is modeled as homogenous broadening with a parabolic spectral dependence, and it is linearly dependent on the carrier number.

$$G_i(N) = G_N(N - N_0)\left[1 - 2\left(i \frac{\Delta\lambda_D}{\Delta\lambda_G} \right)^2 \right] \tag{4.3}$$

where G_N is a gain coefficient, N_0 is the carrier number at transparency, $\Delta\lambda_D$ is the longitudinal mode spacing, and $\Delta\lambda_G$ is the full width at half maximum (FWHM) of the gain curve. The assumption here is that the central mode is located at the gain maximum,

and the wavelength shift with carrier number is neglected. Also the gain width is assumed to be constant.

The recombination rate $R(N)$ is modeled as

$$R(N) = AN + BN^2 + CN^3 \tag{4.4}$$

where the constants *A*, *B*, and *C* represent the recombination via traps or surface states, band-to-band recombination, and Auger recombination, respectively. Only the band-to-band recombination is radiative, and this term is included in Eq. (4.2).

The spontaneous emission coefficient β_i for *i*-th mode is modeled as

$$\beta_i = \frac{\overline{\beta}}{1+\left(i\frac{2\Delta\lambda_D}{\Delta\lambda_S}\right)^2} \tag{4.5}$$

where

$$\overline{\beta} = \frac{\lambda_0^4}{8\pi^2 n_g n_r^2 \Delta\lambda_S V} \tag{4.6}$$

Here $\Delta\lambda_S$ is the FWHM width of the spontaneous emission spectrum, λ_0 is the central wavelength, n_g is the group refractive index, n_r is the refractive index, and V is the mode volume. We assume that the peak of the spontaneous emission is at the same wavelength as the gain spectrum.

The Langevin noise source terms $F_N(t)$ and $F_i(t)$ are assumed to be Gaussian random variables [75]. In the Markov approximation, their autocorrelation and cross correlation functions can be expressed as

$$\left\langle F_N(t')F_N(t'')\right\rangle = V_N^2\delta(t'-t'') \tag{4.7}$$

$$\left\langle F_i(t')F_i(t'')\right\rangle = V_i^2\delta_{ij}\delta(t'-t'') \tag{4.8}$$

$$\left\langle F_N(t')F_i(t'')\right\rangle = r_i V_N V_i\delta(t'-t'') \tag{4.9}$$

where δ_{ij} is the Kronecker delta, and $\delta(t'-t'')$ is the Dirac delta function. V_N^2 and V_i^2 are the variances of F_N and F_i, respectively. r_i is the correlation coefficient. We can see that the photon numbers of different longitudinal modes are not directly related to each other, but interact via the same carrier pool.

Each process term on the right-hand sides of Eq. (4.1) and (4.2) is a source of shot noise, and the total variance of the Langevin noise is the sum of the variances of all the corresponding shot noise. The gain term can be written as the net stimulated emission shown in Eq. (4.10)

$$\Gamma G_i(N) = E_{cv}^i - E_{vc}^i \tag{4.10}$$

where E_{cv}^i is the stimulated emission rate per photon in *i*-th mode, and E_{vc}^i is the absorption rate.

$$E_{cv}^i = \beta_i BN^2 \tag{4.11}$$

Thus, the variances and correlation coefficients can be expressed as

$$V_N^2 = J + R(N) + \sum_i \left(E_{cv}^i + E_{vc}^i\right)S_i \tag{4.12}$$

$$V_i^2 = \left(E_{cv}^i + E_{vc}^i\right)S_i + \frac{1}{\tau_p}S_i + \beta_i BN^2 \tag{4.13}$$

$$r_i V_N V_i = -\left[\left(E_{cv}^i + E_{vc}^i\right) S_i + \beta_i B N^2\right] \tag{4.14}$$

Note that the electron and photon are anti-correlated, thus there is a minus sign in Eq. (4.14). Using Eqs. (4.10) and (4.11), we can derive

$$E_{cv}^i + E_{vc}^i = 2\beta_i B N^2 - \Gamma G_i\left(N\right) \tag{4.15}$$

Substituting Eq. (4.15) into Eqs. (4.12) to (4.14), we can obtain the variances and correlation coefficients as a function of laser parameters.

To numerically solve this noise-driven multi-mode rate equation, we implemented the 4th-order Runge-Kutta method [103]. To handle the Langevin noise, we can express the stochastic function in any time interval Δt as in the study by Marcuse [75]:

$$F_N\left(t\right) = \frac{V_N}{\sqrt{\Delta t}} x_N \tag{4.16}$$

$$F_i\left(t\right) = r_i \frac{V_i}{V_N} F_N + \frac{V_i}{\sqrt{\Delta t}} \sqrt{1 - r_i^2}\, x_i \tag{4.17}$$

where x_N and x_i are independent Gaussian random variables with mean 0 and standard deviation 1. The integration time step is chosen to ensure the convergence of the rate equation, and also to cover the whole frequency spectrum of the laser diode if the fiber dispersion is to be accounted for.

4.3 Mode Probability Density Function and k-factor

In the theoretical analysis of MPN, the total photon number is assumed to remain constant, whereas the photon numbers of the individual modes are randomly fluctuated.

The photon number in the *i*-th mode is normalized by the average total output power as

$$a_i(t) = S_i(t) / \overline{\sum_i S_i(t)} \tag{4.18}$$

where the bar $\overline{\cdot}$ represents the mean value.

k-factor for mode *i* is defined as [72]

$$k_i^2 = \frac{\overline{a_i^2} - \overline{a}_i^2}{\overline{a}_i - \overline{a}_i^2} \tag{4.19}$$

The total k-factor is defined as

$$k^2 = \frac{\sum_i (\overline{a_i^2} - \overline{a}_i^2)}{\sum_i (\overline{a}_i - \overline{a}_i^2)} \tag{4.20}$$

The k-factor is in the range of 0 to 1. A k-factor of 0 means no mode partition, as for the case of LED. A k-factor of 1 is the worst case, where a single mode is lasing, but the frequency varies from the pulse-to-pulse power.

From the statistical analysis of noise, the normalized photon number a_i has a β probability density function (pdf), as expressed in Eq. (4.21) [70].

$$p(a_i) = \frac{a_i^{\left(\xi_i \overline{a_i} - 1\right)} \left(1 - a_i\right)^{\left[\xi_i \left(1 - \overline{a_i}\right) - 1\right]}}{B\left(\xi_i \overline{a_i}, \xi_i \left(1 - \overline{a_i}\right)\right)} \tag{4.21}$$

where $B(x, y)$ is the beta-function, and ξ is a mode partition coefficient

$$\xi_i = \frac{1}{k_i^2} - 1 \tag{4.22}$$

For a real laser, the total photon number also fluctuates instead of being constant. The normalized total photon number a_t has a Gaussian pdf, as

$$p(a_t) = \frac{1}{\sqrt{2\pi}\sigma} \exp\left[-\frac{(a_t - 1)^2}{2\sigma^2} \right] \tag{4.23}$$

where σ is the standard deviation.

For the low-power side mode, the pdf in Eq. (4.21) is approximately exponential distribution, as

$$p(a_i) = \frac{1}{\bar{a}_i} \exp\left[-\frac{a_i}{\bar{a}_i} \right] \tag{4.24}$$

4.4 Simulation

4.4.1 Simulation Setup

The laser parameters follow those in the study by Jensen et al. [102] and are shown in Table 4-1.

RZ code is used, and we modulate the injection current by a square-wave pulse train, with a duty cycle of 0.44. The relaxation frequency is about 2.5 GHz at a bias current of 1.5 times the threshold current (I_{th}). Here we modulate the laser at 2.2 GHz. The time step is 1 ps, and 1024 information pulses are processed. A few more bits are added before and after the information pulse train, to ensure the turn-on of the laser diode, and to avoid hitting the simulation boundary. Eleven modes are calculated.

Table 4-1 Laser parameters [102]

Parameter	Symbol	Value
Nonradiative recombination constant	A	$1\times10^{8}\ s^{-1}$
Band-to-band recombination constant	B	$0.26\ s^{-1}$
Auger recombination constant	C	$4.44\times10^{-10}\ s^{-1}$
Photon lifetime	τ_p	2 ps
Mode confinement factor	Γ	0.3
Carrier number at transparency	N_0	3×10^{8}
Longitudinal mode spacing	$\Delta\lambda_D$	0.72 nm
Width of gain curve	$\Delta\lambda_G$	32.5 nm
Width of spontaneous emission spectrum	$\Delta\lambda s$	50.0 nm
Gain coefficient	G_N	$3.3\times10^{3}\ s^{-1}$
Center wavelength	λ_0	1.3 μm
Group refractive index	n_g	3.9
Refractive index	n_r	3.3
Mode volume	V	$3\times10^{-16}\ m^{3}$

A low-pass filter is used after the laser diode photon output to emulate the receiver. Its 3dB bandwidth is set to be equal to the modulation frequency, and the impulse response is

$$h(k)=\begin{cases}\sin^2\left(\pi\dfrac{k}{K}\right), & \text{k = 0,1,...,K}\\ 0, & \text{elsewhere}\end{cases} \tag{4.25}$$

After the low-pass filter, we find the sampling time point in the pulse interval where the total photon number is maximal when Langevin noise is turned off. We then sample the photon number of each mode at this instant.

From the sampled data, we can calculate the pdf. The photon number samples are collected in 200 bins, and then the sample number in each bin is divided by the total number of samples. The k-factor can also be calculated using Eqs. (4.19) and (4.20) from the sampled data. Note that we only count in bits '1' information, since the assumption in the analytical derivation was that the total photon number is constant from pulse to pulse [70].

4.4.2 Mode pdf Results

We conducted the simulation for the modulation frequency of 2.2 GHz, with bias current I_{bias} = 1.05 × I_{th}, and the pulse current I_{pulse} = 0.45 × I_{th}. 1024 pulses, all of which are bits '1', are simulated with Langevin noise on.

Figure 4-1 shows the average mode spectrum over the sampled photon numbers. The root-mean-square (RMS) width is 0.92 nm.

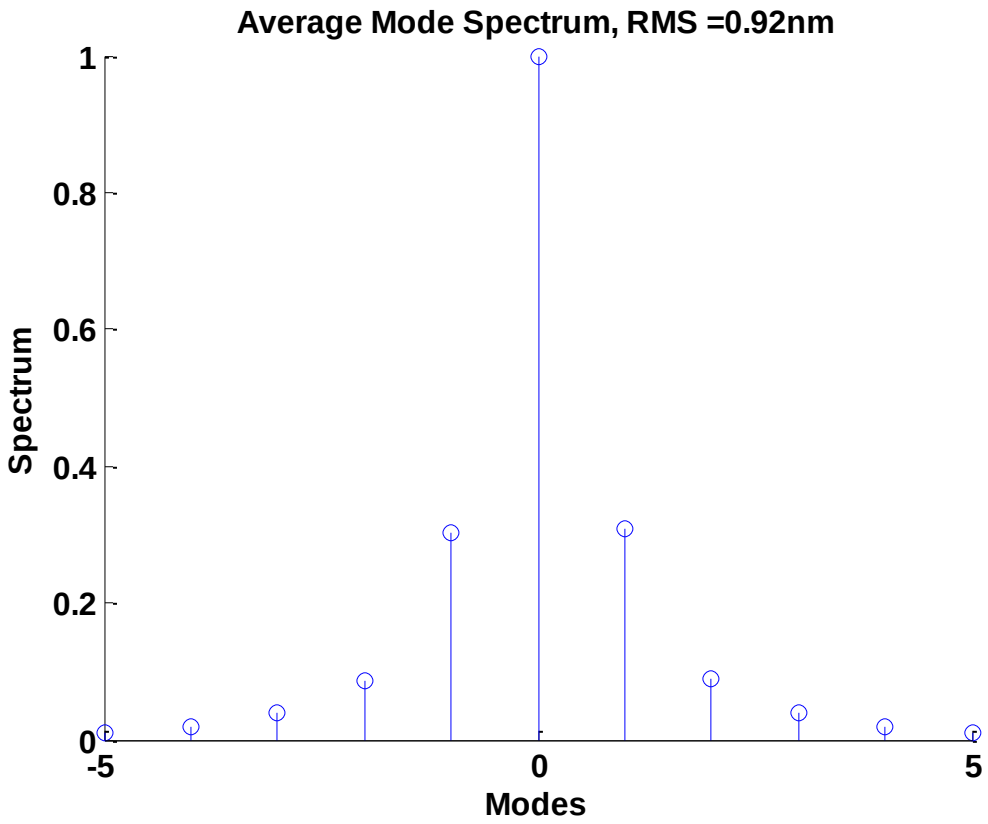

Figure 4-1 Average longitudinal mode spectrum under pulsed modulation. Modulation frequency is 2.2 GHz, I_{bias} = 1.05 × I_{th}, I_{pulse} = 0.45 × I_{th}. This is the average over the sampled data of 1024 pulses of bits '1'.

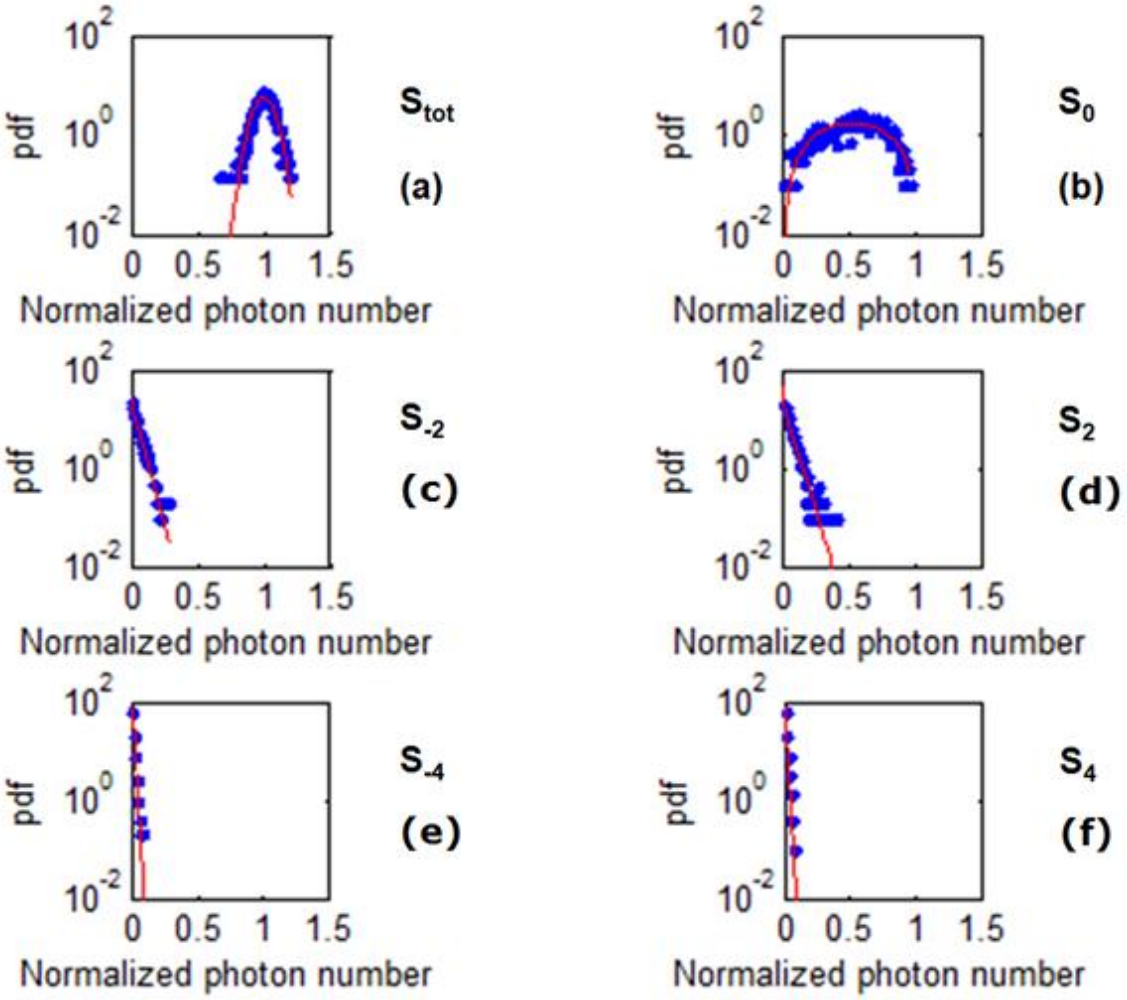

Figure 4-2 Probability density functions for (a) the total photon output S_{tot}, (b) the central mode S_0, and a few side modes (c) S_{-2}, (d) S_2, (e) S_{-4}, (f) S_4. The blue dots are pdf calculated from counting the sample numbers in bins, and the red solid lines are the fitted curve to the analytical formulas.

Figure 4-2 illustrates the probability density functions for (a) the total photon output S_{tot}, (b) the central mode S_0, and a few side modes (c) S_{-2}, (d) S_2, (e) S_{-4}, (f) S_4. The pdf calculated from counting the sample numbers in bins are shown in blue dots, and the red solid lines are the fitted curve to the theoretical formulas in Eqs. (4.21), (4.23) and (4.24). The simulation results are in good agreement with the literature [102], and fit well with the theoretical curves. We can see that the total photon output S_0 has a Gaussian distribution instead of being a constant as expected, and the modal pdf match well with predicted distributions although the analyze was based on the assumption of a constant total power. The pdf for each mode is well fitted with the Beta distribution (S_0, S_{-2}, and S_2), and the low-power side mode shows an exponential distribution (S_{-4} and S_4).

Our simulation results agree with the published results [102], which validates our simulation model.

4.4.3 k-factor Results

The k-factor describes the degree of power fluctuations in each longitudinal mode of the FP laser. For a multi-mode FP laser, the power fluctuations are induced by two sources: one is the laser Langevin noise that randomly varies the power, and can be called “intrinsic”; the other one is the bit pattern effect which is deterministic and has a memory effect, and can be referred as “extrinsic”. Therefore, to make k-factor zero, two conditions are required: 1) the intrinsic laser Langevin noise must be turned off; and 2) the bit pattern must be regular, not random.

To study the contribution of these two sources, we simulate the same laser diode and low-pass filter. The modulation frequency is still 2.2 GHz, with bias current I_{bias} = 1.05 × I_{th}, and the modulation pulse current I_{pulse} = 0.45 × I_{th}. 1024 pulses are calculated. Four different conditions are simulated: 1) Regular bit pattern, Langevin noise are turned off; 2) Regular bit pattern, Langevin noise are turned on; 3) Random bit pattern, Langevin noise are turned off; and 4) Random bit pattern, Langevin noise are turned on. Since we use RZ code, for regular bit pattern, all the bits are set to '1'. For random bit pattern, we use the De Bruijn sequence to efficiently traverse all the combinations of sequence.

Figure 4-3 shows the waveform for total photon number and major modes when all bits are '1's, and without Langevin noise. (a) is the laser diode output, and (b) is the waveform after the low-pass filter. There is no power fluctuation at all; thus the sampled data are all the same, as shown by the straight lines in Figure 4-4. Therefore, the k-factor is calculated to be 0.

Figure 4-5 shows the waveform for total photon number and major modes when all bits are '1's, and with Langevin noise. (a) is the laser diode output, and (b) is the waveform after the low-pass filter. The sampled photon output is shown in Figure 4-6. We can see that the Langevin noise causes the mode power to randomly change. The total k-factor is calculated to be 0.36, and the k-factor for each mode is illustrated in Figure 4-7. The k-factors for the central modes are larger, and the k-factors for the low-power side modes are smaller.

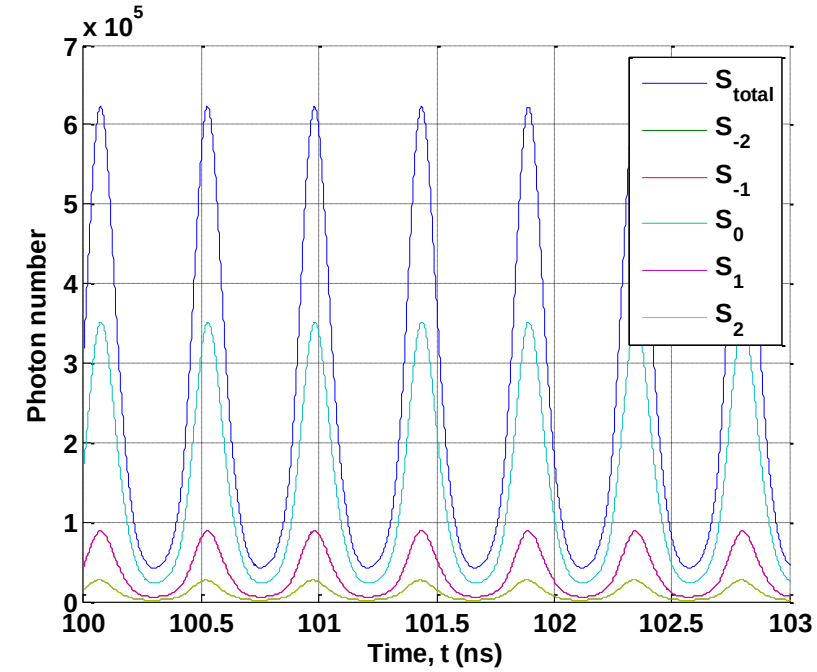

(a)

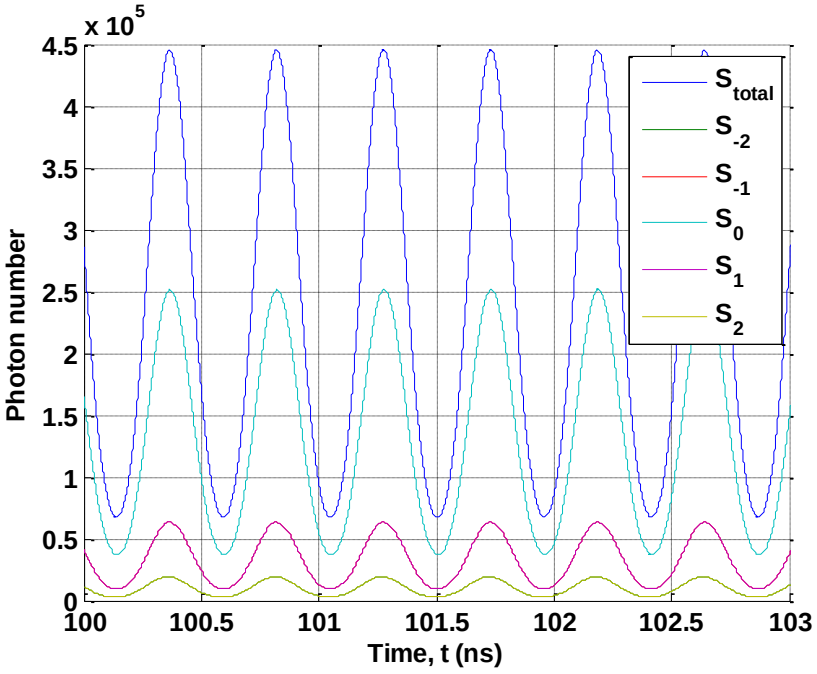

(b)

Figure 4-3 The waveform for total photon number and major modes. All bits are ‘1’s, and without Langevin noise. (a) Laser diode output. (b) After the low-pass filter.

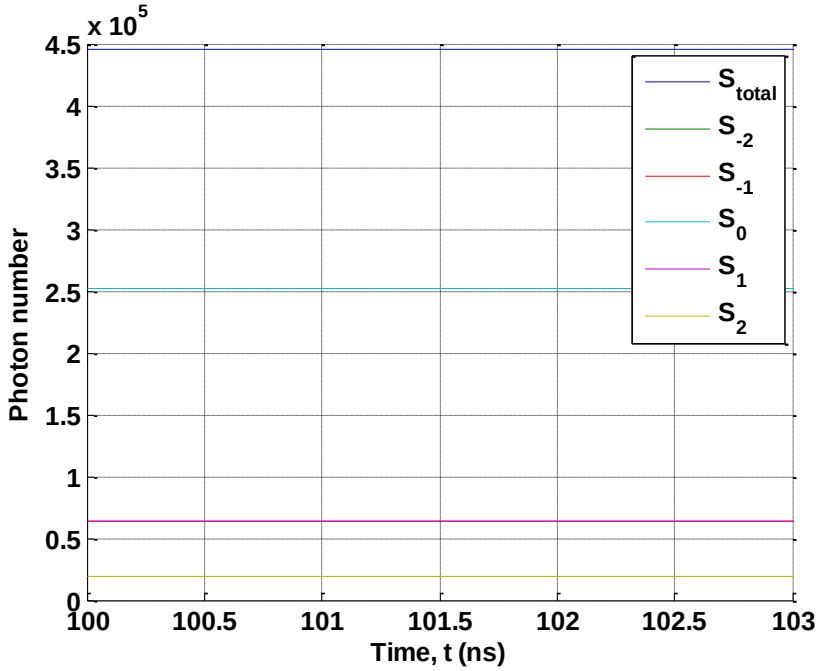

Figure 4-4 The sampled waveform for total photon number and major modes. All bits are ‘1’s, without Langevin noise.

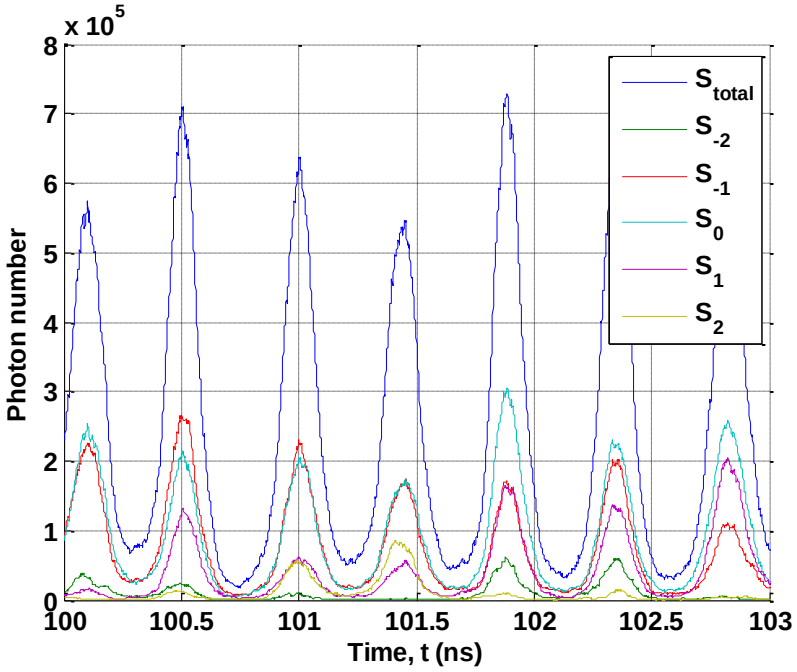

(a)

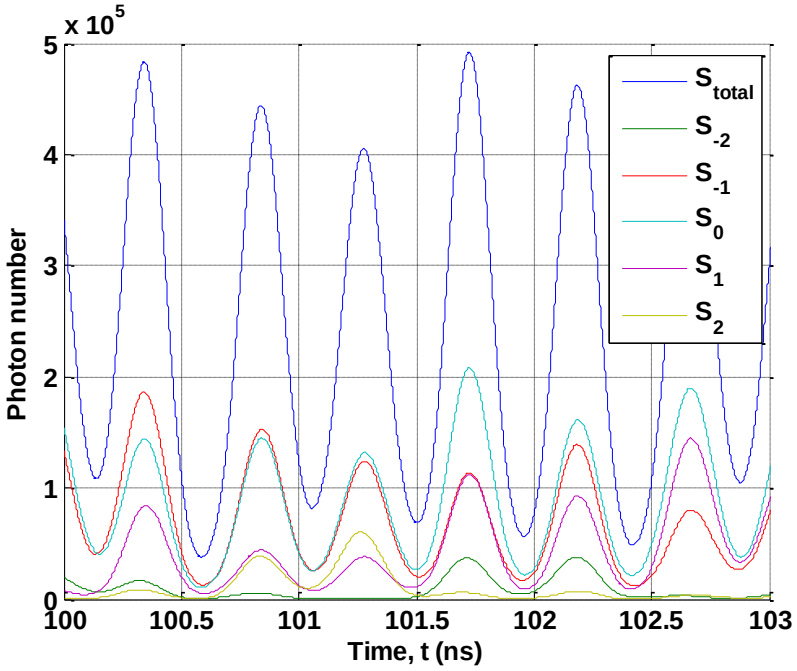

(b)

Figure 4-5 The waveform for total photon number and major modes. All bits are '1's, with Langevin noise. (a) Laser diode output. (b) After the low-pass filter.

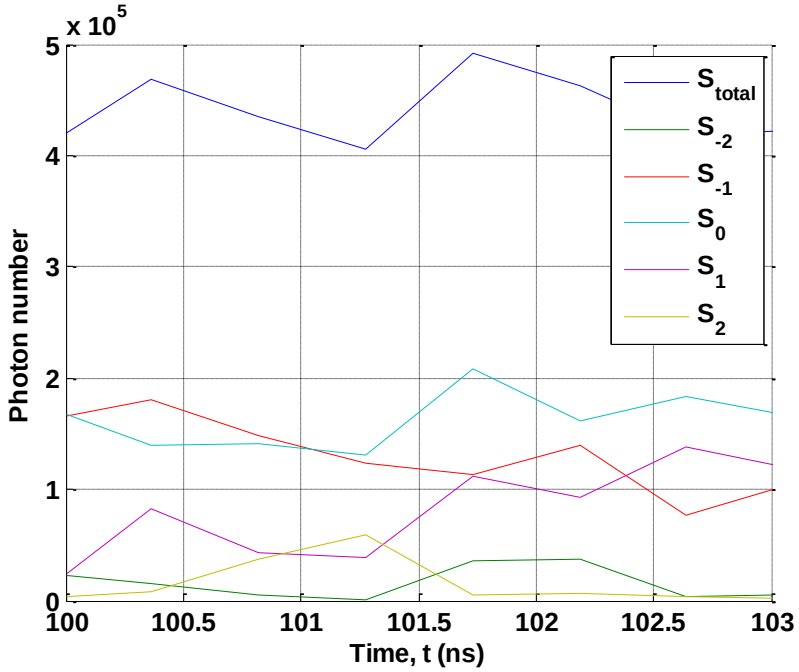

Figure 4-6 The sampled waveform for total photon number and major modes. All bits are ‘1’s, with Langevin noise.

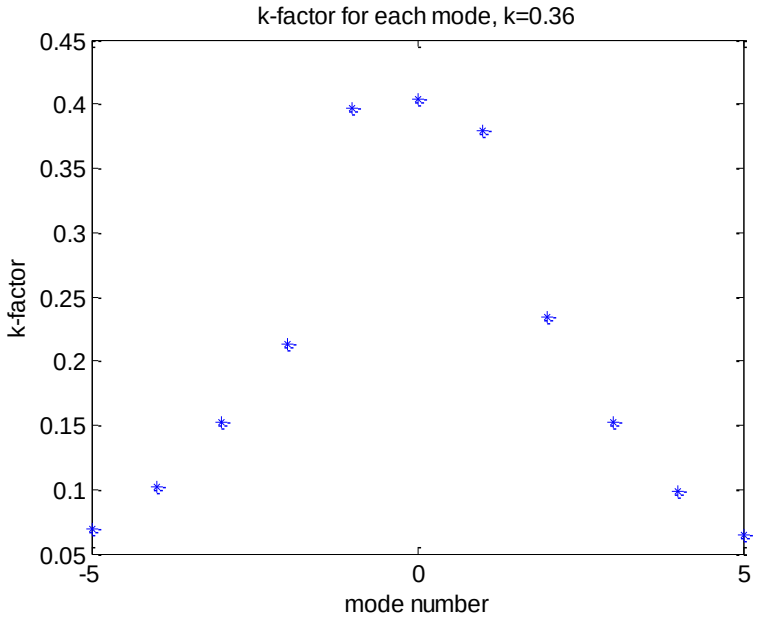

Figure 4-7 k-factor for each mode. All bits are ‘1’s, with Langevin noise.

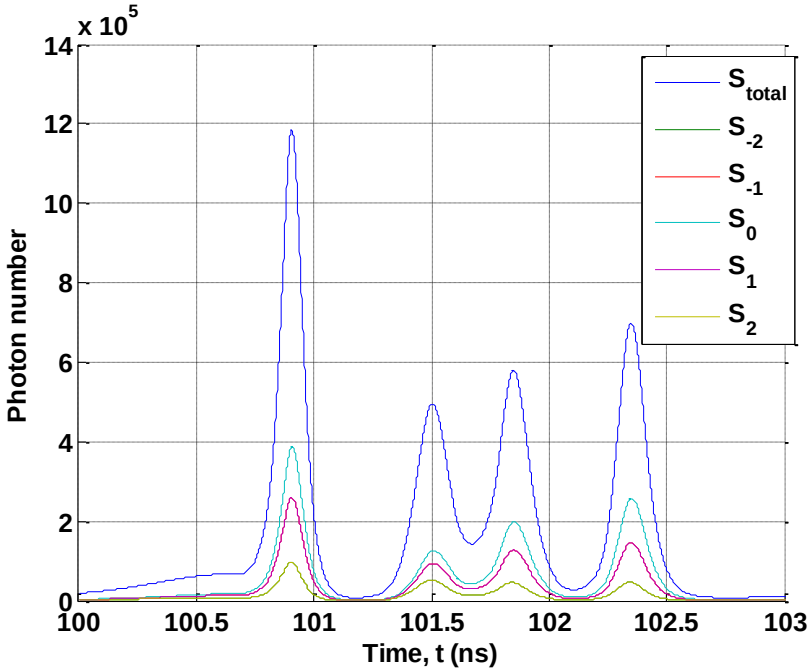

(a)

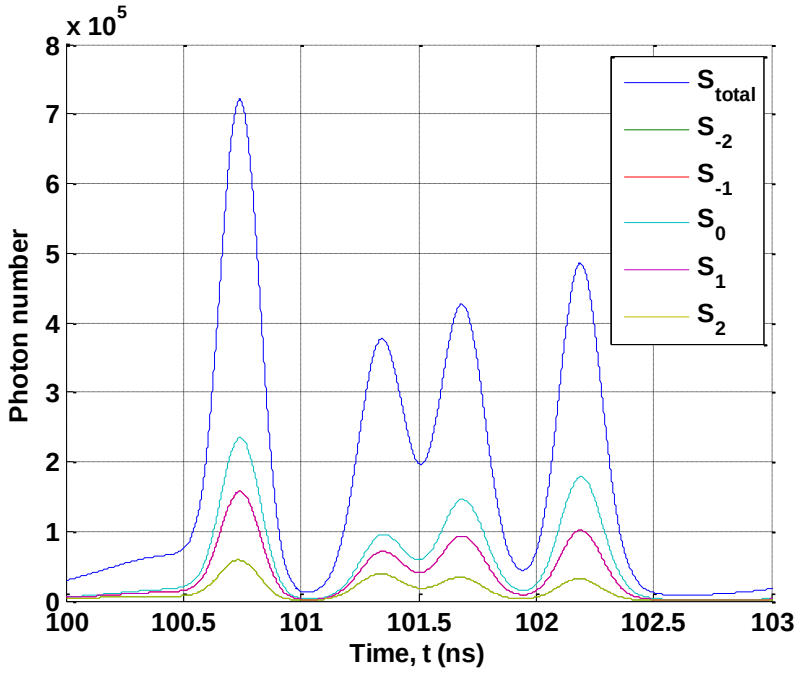

(b)

Figure 4-8 The waveform for total photon number and major modes. The bit pattern is De Bruijn sequence, without Langevin noise. (a) Laser diode output. (b) After the low-pass filter.

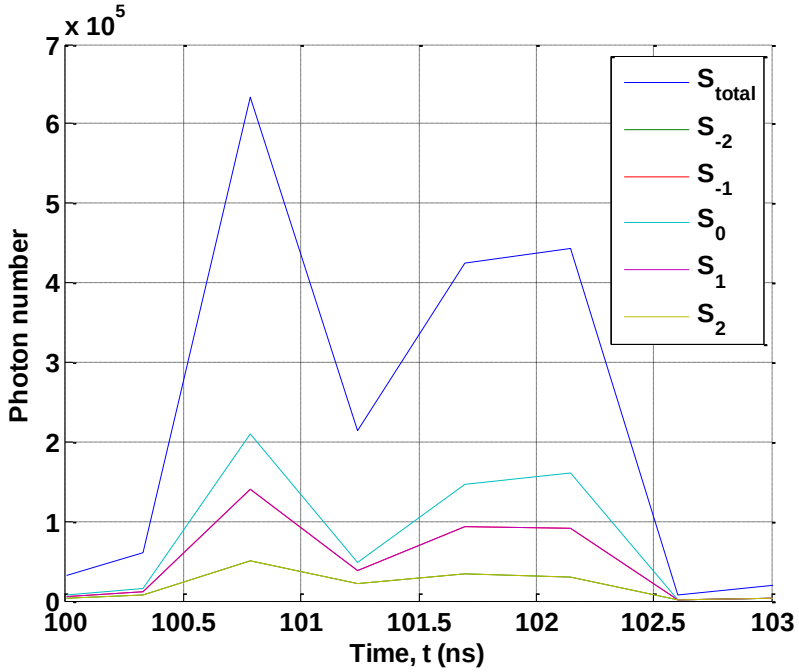

Figure 4-9 The sampled waveform for total photon number and major modes. The bit pattern is De Bruijn sequence, without Langevin noise.

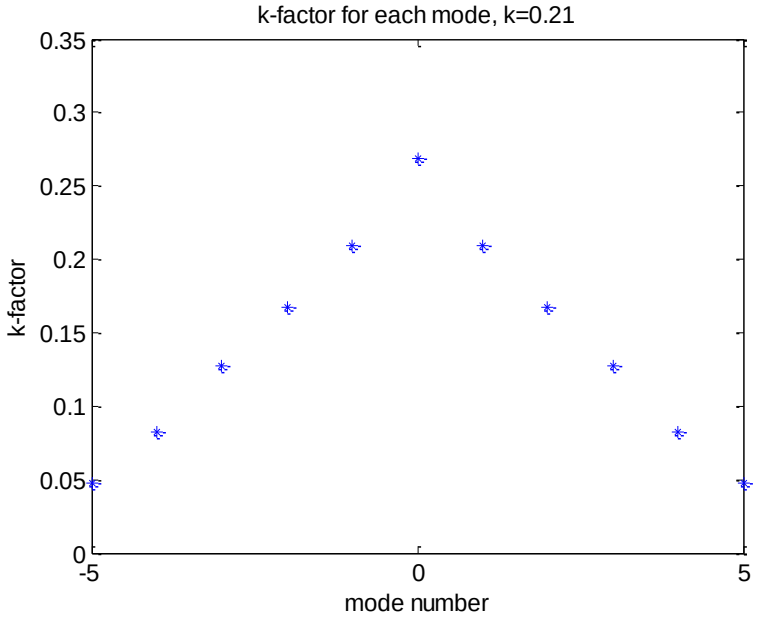

Figure 4-10 k-factor for each mode. The bit pattern is De Bruijn sequence, without Langevin noise.

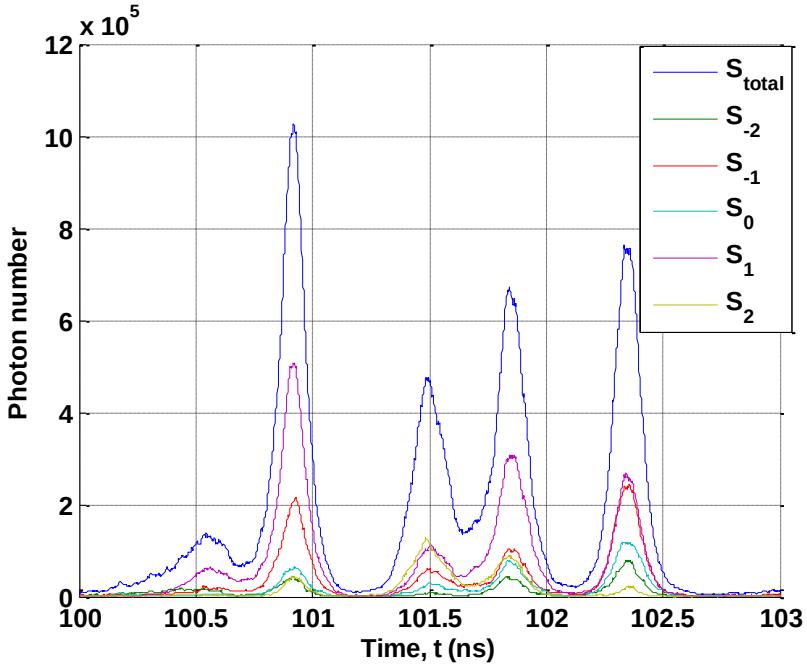

(a)

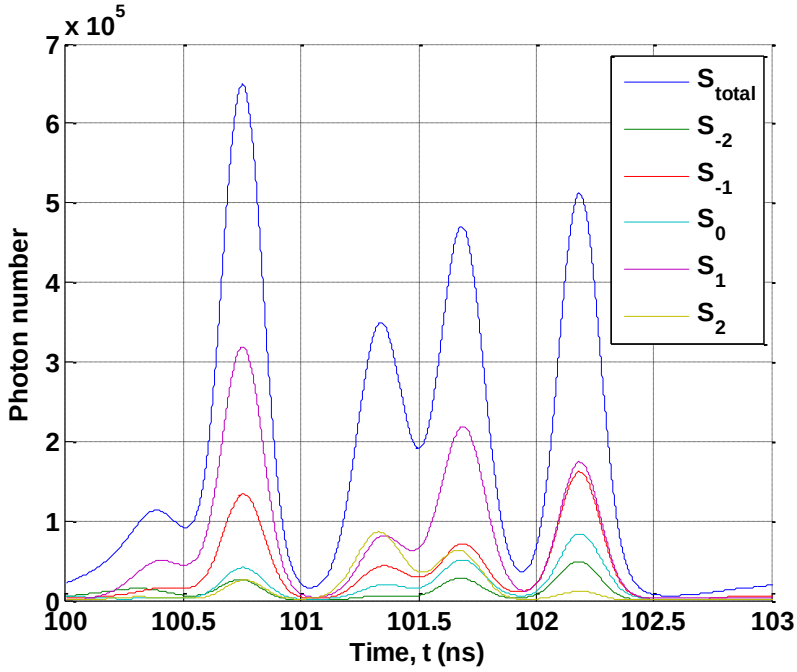

(b)

Figure 4-11 The waveform for total photon number and major modes. The bit pattern is De Bruijn sequence, with Langevin noise. (a) Laser diode output. (b) After the low-pass filter.

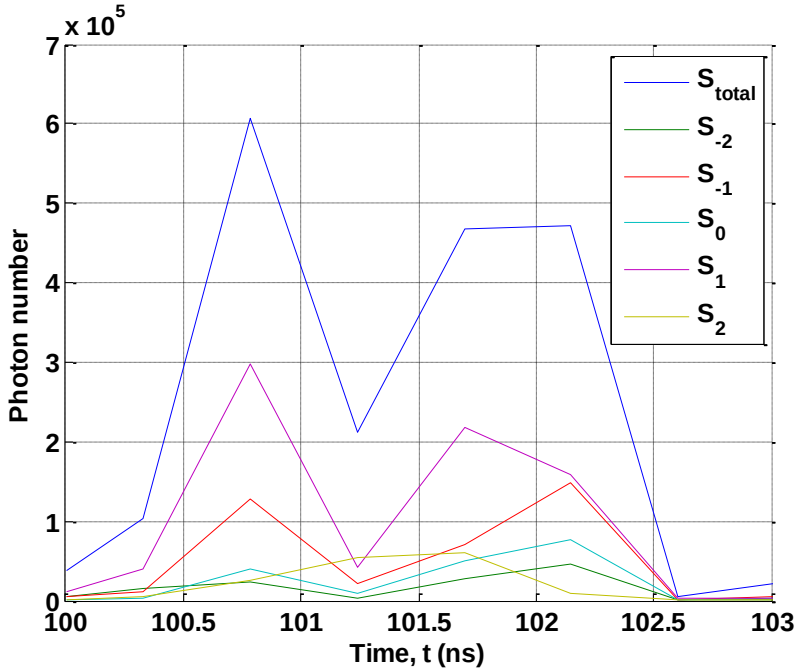

Figure 4-12 The sampled waveform for total photon number and major modes. The bit pattern is De Bruijn sequence, with Langevin noise.

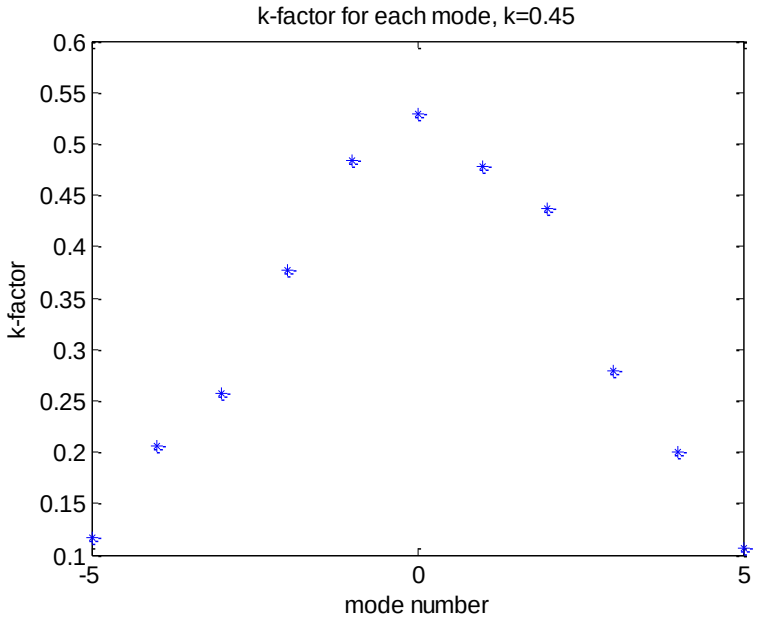

Figure 4-13 k-factor for each mode. The bit pattern is De Bruijn sequence, with Langevin noise.

Figure 4-8 shows the waveform for total photon number and major modes for the bit pattern of De Bruijn sequence, and without Langevin noise. Again (a) is the laser diode output, and (b) is the waveform after the low-pass filter. The sampled photon output is shown in Figure 4-9. We can see that without the laser Langevin noise, the bit pattern itself can cause the laser power to vary with time. The total k-factor is 0.21, and the k-factor for each mode is illustrated in Figure 4-10. High-power mode has larger k-factor.

Finally, both sources are included in the simulation. This should introduce the biggest power fluctuations. The bit pattern is De Bruijn sequence, and the Langevin noise is turned on. Figure 4-11 shows the waveform (a) at the laser diode output, and (b) after the low-pass filter. Figure 4-12 is the sampled data, and Figure 4-13 shows the k-factor for each mode. The total k-factor is 0.45, and high-power mode has larger k-factor.

We can denote the total k-factor as k_1, k_2, k_3 and k_4 for the four simulation conditions:

1. {Regular bit pattern, without Langevin noise}, represented by k_1
2. {Regular bit pattern, with Langevin noise}, represented by k_2
3. {Random bit pattern, without Langevin noise}, represented by k_3
4. {Random bit pattern, with Langevin noise}, represented by k_4

It can be seen from the previous results that $k_1 = 0$, $k_2 > 0$, $k_3 > 0$, $k_4 > k_2$, and $k_4 > k_3$, as expected. The value $k_4 \sim \sqrt{k_2^2 + k_3^2}$ approximately.

Next, the k-factors at different operating conditions are studied. For each case, the k-factors of four simulation conditions are calculated and plotted in figures, and the value $\sqrt{k_2^2 + k_3^2}$ is also computed for reference. Blue circles represent k_1; green upward-pointing triangles represent k_2; red downward-pointing triangles represent k_3; cyan asterisks represent k_4; and magenta plus signs represent $\sqrt{k_2^2 + k_3^2}$.

In Figure 4-14, the modulation current I_{pulse} is kept constant as $0.45 \times I_{th}$, and bias current I_{bias} is varied at $\{0.95, 1.05, 1.5, 2.0\} \times I_{th}$. It can be seen that the total k-factors and contributions from Langevin noise and bit pattern randomness all decrease with increasing bias current. The contribution of Langevin noise to the k-factor is bigger than that of the random bit pattern, and is more dominant at lower bias current.

In Figure 4-15, the bias current I_{bias} is kept constant as $1.05 \times I_{th}$, while the modulation current I_{pulse} is varied at $\{0.45, 0.75, 1.05\} \times I_{th}$. It can be seen that the total k-factors decrease slightly with increasing pulse current, and the contribution of bit pattern randomness decreases. The contribution of Langevin noise to the k-factor is also bigger than that of the random bit pattern, and is more dominant at higher modulation current.

In Figure 4-16, the average injection current is kept as a constant. With the increasing bias current and decreasing pulse current, the contribution of Langevin noise to the k-factor decreases, and the contribution from random bit pattern slightly increases. The contribution of Langevin noise to the k-factor is still bigger than that of the random bit pattern, and is more dominant at lower bias current.

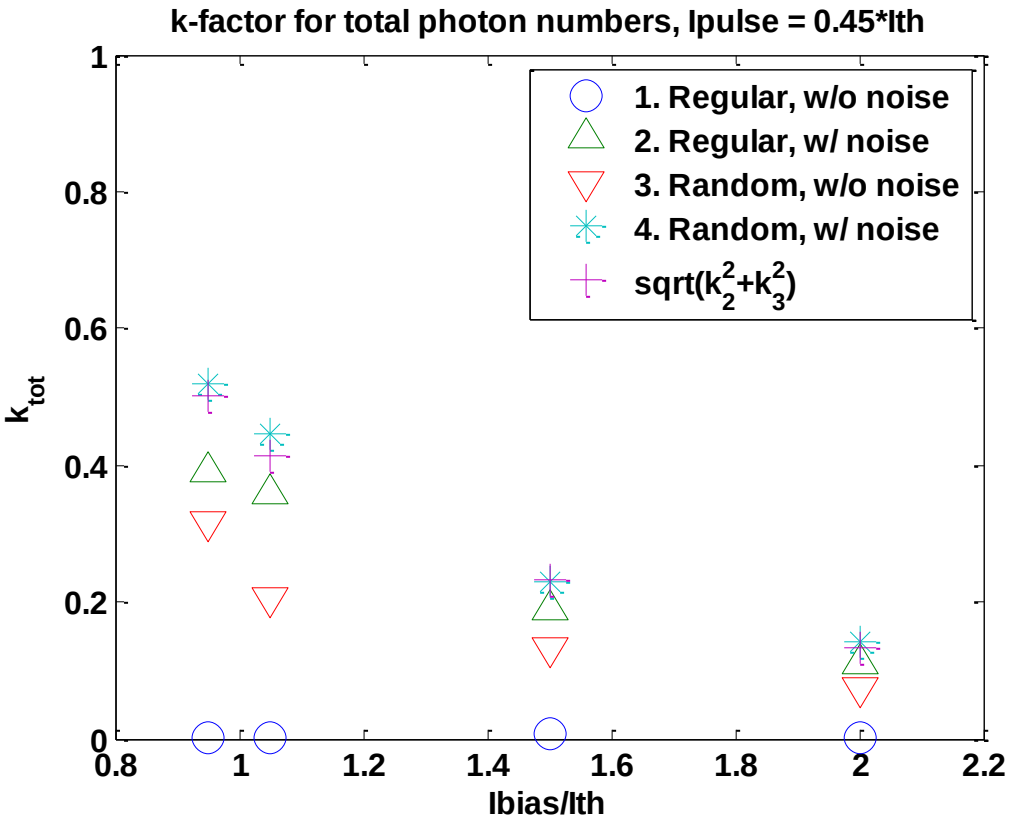

Figure 4-14 The total k-factor for four simulation conditions. The modulation current I_{pulse} is kept constant as $0.45 \times I_{th}$, and bias current I_{bias} is varied at $\{0.95, 1.05, 1.5, 2.0\} \times I_{th}$.

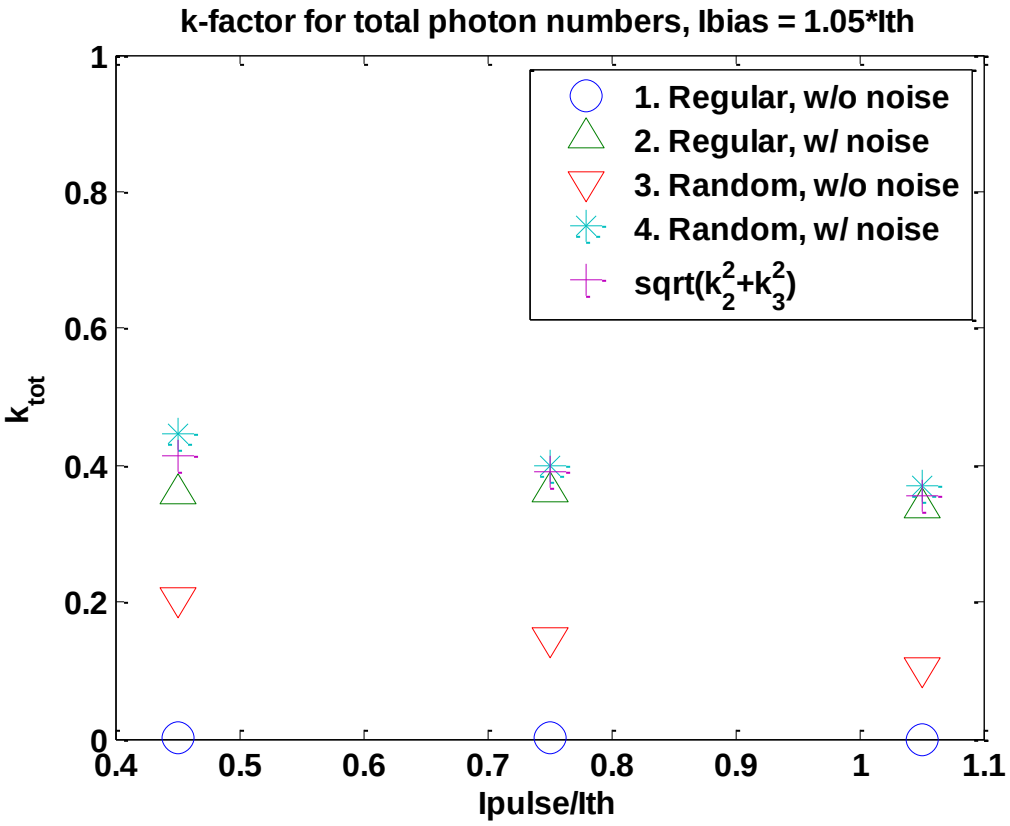

Figure 4-15 The total k-factor for four simulation conditions. The bias current I_{bias} is kept constant as $1.05 \times I_{th}$, while the modulation current I_{pulse} is varied at $\{0.45, 0.75, 1.05\} \times I_{th}$.

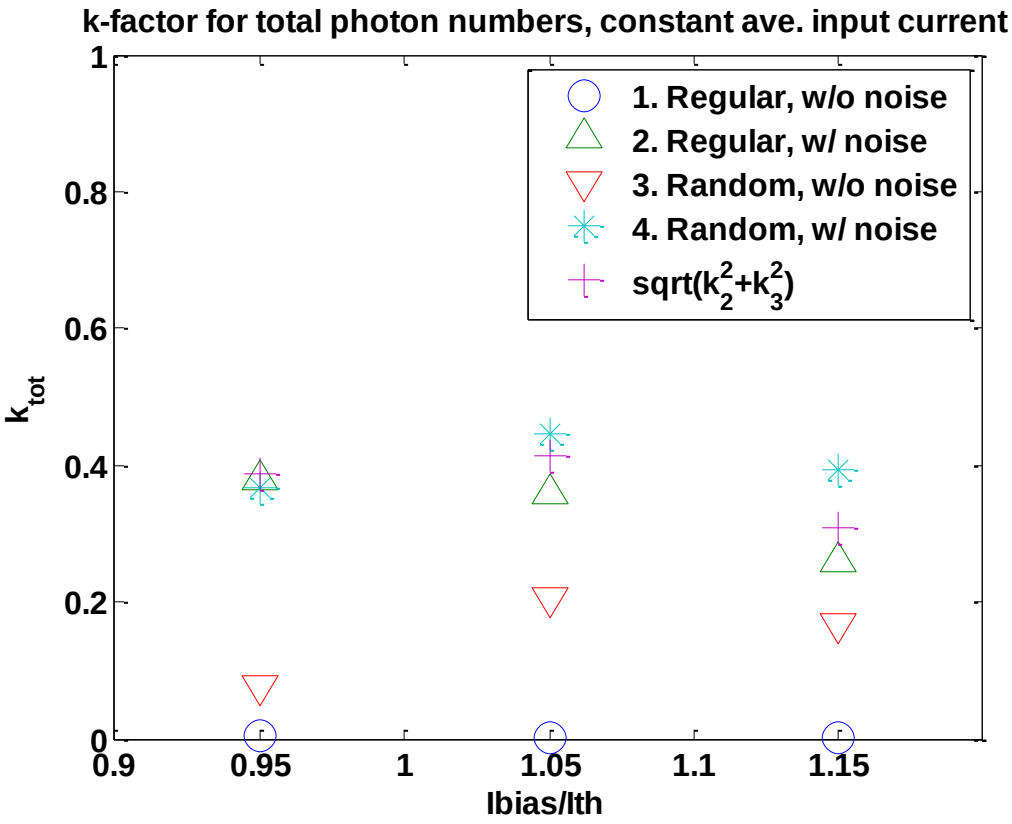

Figure 4-16 The total k-factor for four simulation conditions. The average injection current is kept as a constant.

4.5 Summary

In this chapter, we have studied the MPN characteristics of FP laser diode using the time-domain simulation of noise-driven multi-mode laser rate equation. The probability density functions are calculated for each mode. The sources of the k-factor are investigated with simulation, including the intrinsic source of the laser Langevin noise, and the extrinsic source of the bit pattern. The photon waveforms are shown under four simulation conditions for regular/random bit pattern, and with/without Langevin noise. The k-factors contributed by those sources are studied with a variety of bias current and modulation current.

Chapter 5.

Summary and Future Work

5.1 Contributions of the Thesis

Passive optical network (PON) is considered as the most appealing access network architecture in terms of cost-effectiveness, bandwidth management flexibility, scalability and durability. The overall objectives of this thesis are the investigation of cost-effective and high-performance designs of link system and devices in the PON.

Firstly, a novel optical orthogonal frequency division multiplexing (OOFDM)-PON upstream link scheme is proposed and numerically simulated with two configurations: 10 Gbit/s bit rate for 4 optical network units (ONUs), and 2.5 Gbit/s bit rate for 16 ONUs. At the ONUs, orthogonal subcarrier multiplexing is used to realize colorless ONU and high spectral efficiency. At the optical line terminal (OLT), the optical switch and all optical fast Fourier transform (OFFT) are applied to achieve high speed demultiplexing. According to the Monte-Carlo simulation results of the BER, the tolerance of the laser diode central wavelength shift in ONUs for 10 Gbit/s link is higher than that for the 2.5 Gbit/s link.

Next, we design and numerically simulate a newly proposed polarization beam splitter (PBS) device based on a planar waveguide platform. PBS is one of the most important components in polarization-controlled optical systems, e.g. the next-generation

PON utilizing polarization multiplexing. In our PBS design, a wedge made of a subwavelength grating utilizes the form birefringence to enlarge the effective refractive index difference between the TM and TE polarizations, and splits the two polarization beams to different directions. The insertion loss is less than 0.9 dB for the designed operating wavelength band of 1.5 μm to 1.6 μm. The crosstalk between the two polarizations is below -30 dB. The whole device size is 300 μm × 80 μm, and can potentially be further reduced by improving the lens design. This PBS device can be readily fabricated by lithography and etching, and can be monolithically integrated with other optical components on the same platform. This design can also be extended to other material systems and other wavelength bands to meet the required specifications.

Lastly, we study the mode partition noise (MPN) characteristics of the Fabry-Perot (FP) laser diode using the time-domain simulation of noise-driven multi-mode laser rate equation. FP laser is cheaper than the widely used distributed feedback (DFB) laser diode in PON, but its MPN is the major limiting factor in an optical transmission system. We calculate the probability density functions for each longitudinal mode. The sources of the k-factor are studied with simulation, including the intrinsic source of the laser Langevin noise, and the extrinsic source of the bit pattern. The photon waveforms are shown under four simulation conditions for regular/random bit pattern, and with/without Langevin noise. The k-factors contributed by those sources are studied with a variety of bias current and modulation current.

Publications

1. Q. Guo, K. He, X. Li, and W.-P. Huang, "A novel upstream link scheme for OOFDM-PON," *IEEE Access Networks and In-house Communications (ANIC) Topical Meeting*, Toronto, Ontario, Canada, Jun. 2011, paper AMC2.
2. Q. Guo, X. Li, J. Mu, L. Han and W.-P. Huang, "Planar waveguide polarization beam splitter based on the form birefringence," *IEEE Photonics Technology Letters*, vol. 24, no. 20, pp. 1034-1037, Oct. 2012.

5.2 Future Work

When multi-mode FP laser is used as the transmitter, fiber-dispersion-induced inter-symbol interference (ISI) will be enhanced due to MPN. Some of our primitive simulations show that maximum-likelihood sequence estimation (MLSE) receiver may reduce the bit error rate (BER) and MPN penalty induced by the bit pattern randomness. After training, the MLSE receiver has a better performance than an optimum-threshold-based direct-detection receiver when mode hopping is absent. MLSE does not mitigate Langevin-noise-induced MPN penalty; therefore, we do not expect a significant performance improvement when the contribution of Langevin noise to the k-factor is dominant. Further simulations and investigations need to be conducted to illustrate quantitatively the effective optical gain of MLSE receiver as a function of laser intrinsic parameters and operating conditions.

In the time-domain numerical simulation, mode hopping/switching can be observed even when the FP laser is operated with DC current. The probability and frequency of mode hopping is related to laser design parameters and Langevin noise. When mode hopping happens, the system performance will be severely affected, and MLSE receiver will not work without re-training. Therefore, it would be interesting and significant to find an easily-implemented design to suppress mode hopping in FP laser.

References

[1] L. Pavesi, “Routes toward silicon-based lasers”, *Materials Today*, vol. 8, pp.18-25, Jan. 2005.

[2] S. Coffa, “Light from silicon”, *IEEE Spectrum*, vol. 42, pp. 44-49, Oct. 2005.

[3] S.-H. Yen, S.-W. Wong, S. Das, N. Cheng, J. Cho, S. Yamashita, O. Solgaard, and L. G. Kazovsky, "Photonic components for future fiber access networks," *IEEE J. Sel. Areas Commun.*, vol. 28, pp. 928-935, Aug. 2010.

[4] W.-P. Huang, X. Li, C.-Q. Xu, X. Hong, C. Xu, and W. Liang, “Optical transceivers for fiber-to-the-premises applications: system requirements and enabling technologies,” *J. Lightwave Technol.*, vol. 25, pp. 11-27, Jan. 2007.

[5] G. Kramer, *Ethernet Passive Optical Networks*, McGraw-Hill, 2005.

[6] K. Choi, J. Moon, J. H. Lee, and C. Lee, “An efficient evolution method from a TDM-PON with a video overlay to NGA,” *Proc. OFC 2008*, paper OWH1, 2008.

[7] H. D. Kim, S.-G. Kang and C.-H. Lee, “A low-cost WDM source with an ASE injected Fabry-Perot semiconductor laser,” *IEEE Photon. Technol. Lett.*, vol. 12, pp. 1067-1069, Aug. 2000.

[8] A. Borghesani, I. F. Lealman, A. Poustie, D. W. Smith, and R. Wyatt, “High temperature, colourless operation of a reflective semiconductor optical amplifier for 2.5Gbit/s upstream transmission in a WDM-PON”, *2007 33rd European Conference on Optical Communication (ECOC)*, pp. 1-2, Sep. 2007.

[9] G. C. Yang and W. C. Kwong, "Performance comparison of multiwavelength CDMA and WCDMA+CDMA for fiber optic network," *IEEE Trans. Commun*., vol. 45, pp. 1426, Nov. 1992.

[10] K. Takiguchi, T. Shibata and H. Takahashi, "Time-spreading/wavelength hopping OCDMA experiment using PLC encoder/decoder with large spread factor," *Electron. Lett.*, vol. 42, pp. 301 – 302, Mar. 2006.

[11] J.-M. Kang and S.-K. Han, "A novel hybrid WDM/SCM-PON sharing wavelength for up- and down-link using reflective semiconductor optical amplifier," *IEEE Photon. Technol. Lett*., vol. 18, pp. 502-504, Feb. 2006.

[12] T. E. Darcie, "Subcarrier multiplexing for lightwave networks and video distribution system," *IEEE J. Sel. Areas Commun.*, vol. 8, pp. 1240-1248, Sep. 1990.

[13] D. Qian, N. Cvijetic, J. Hu, and T. Wang, "A novel OFDMA-PON architecture with source-free ONUs for next-generation optical access networks", *IEEE Photon. Technol. Lett*., vol. 21, pp. 1265-1267, Sep. 2009.

[14] Y.-M. Lin and P.-L. Tien, "Next-generation OFDMA-based passive optical network architecture supporting radio-over-fiber," *IEEE J. Sel. Areas Commun.*, vol. 28, pp. 791-799, Aug. 2010.

[15] *Carrier Sense Multiple Access with Collision Detection (CSMA/CD) Access Method and Physical Layer Specifications-Amendment: Media Access Control Parameters, Physical Layers, and Management Parameters for Subscriber Access Networks*, IEEE Standard 802.3ah, 2004.

[16] ITU-T Recommendation G.984.1, “Gigabit-capable Passive Optical Networks (G-PON): General characteristics,” 2003.

[17] *Carrier Sense Multiple Access with Collision Detection (CSMA/CD) Access Method and Physical Layer Specifications-Amendment: Physical Layers Specifications and Management Parameters for 10 Gb/s Passive Optical Networks*, IEEE Standard 802.3av, 2009.

[18] ITU-T Recommendation G.987.1, “10Gigabit-capable Passive Optical Networks (XG-PON): General requirements,” 2009.

[19] J.-i. Kani, "Enabling Technologies for Future Scalable and Flexible WDM-PON and WDM/TDM-PON Systems," *IEEE J. Sel. Topics Quantum Electron.*, vol. 16, pp. 1290-1297, Sep./Oct. 2010.

[20] J. Armstrong, "OFDM for optical communications," *J. Lightwave Technol*., vol. 27, pp. 189-204, Feb. 2009.

[21] W. Shieh and I. Djordjevic, *Orthogonal frequency division multiplexing for optical communications*, Elsevier Inc., 2010.

[22] W. Shieh, H. Bao, and Y. Tang, "Coherent optical OFDM: theory and design," *Opt. Express*, vol. 16, pp. 841-859, Jan. 2008.

[23] C. W. Chow, C. H. Yeh, C. H. Wang, C. L. Wu, S. Chi, and C. Lin, "Studies of OFDM signal for broadband optical access networks," *IEEE J. Sel. Areas Commun.*, vol. 28, pp. 800-807, Aug. 2010.

[24] D. Qian, N. Cvijetic, J. Hu, and T. Wang, "108 Gb/s OFDMA-PON with polarization multiplexing and direct detection," *J. Lightwave Technol*., vol. 28, pp. 484-493, Feb. 2010.

[25] Y. Li, Y. Xi, X. Li, and W.-P. Huang, "Design and analysis of single mode Fabry-Perot lasers with high speed modulation capability," *Opt. Express*, vol. 19, pp. 12131-12140, Jun. 2011.

[26] K. Nakahara, E. Nomoto, T. Tsuchiya, Y. Katou, R. Kaneko, and A. Taike, "A 4 km transmission at 10-Gb/s operation with wide temperature range in 1.3-μm InGaAlAs MQW FP lasers," *IEEE 18th International Semiconductor Laser Conference*, pp. 59-60, 2002.

[27] Y. Yi, S. Verschuere, Z. Lou, P. Ossieur, J. Bauwelinck, X.-Z. Qiu, and J. Vandewege, "Simulations and experiments on the effective optical gain of FEC in a GPON uplink," *IEEE Photon. Technol. Lett*., vol. 19, pp. 82-84, Jan. 2007.

[28] J. M. Oh, S. G. Koo, D. Lee, and S. J. Park, "Enhancement of the performance of a reflective SOA-based hybrid WDM/TDM PON system with a remotely pumped erbium-doped fiber amplifier," *IEEE J. Lightw. Technol*., vol. 26, pp. 144–149, Jan. 2008.

[29] J. Kani and K. Iwatsuki, "A wavelength-tunable optical transmitter using semiconductor optical amplifiers and an optical tunable filter for metro/access DWDM applications," *IEEE J. Lightw. Technol*., vol. 23, pp. 1164–1169, Mar. 2005.

[30] S. Hara and R. Prasad, *Multicarrier Techniques for 4G Mobile Communications*, Artech House Publishers, 2003.

[31] L. Hanzo and T. Keller, *OFDM and MC-CDMA: A Primer*, IEEE Press, 2006.

[32] Q. Pan and R. J. Green, "Bit-error-rate performance of lightwave hybrid AM/OFDM systems with comparison with AM/QAM systems in the presence of clipping impulse noise," *IEEE Photon. Technol. Lett*., vol. 8, pp. 278-280, Feb. 1996.

[33] W. Shieh and C. Athaudage, "Coherent optical orthogonal frequency division multiplexing," *Electron. Lett*., vol. 42, pp. 587-589, May 2006.

[34] I. Djordjevic and B. Vasic, "Orthogonal frequency division multiplexing for high-speed optical transmission," *Opt. Express*, vol. 14, pp. 3767-3775, May 2006.

[35] H. Bao and W. Shieh, "Transmission simulation of coherent optical OFDM signals in WDM systems," *Opt. Express*, vol. 15, pp. 4410-4418, Apr. 2007.

[36] Y. Tang, W. Shieh, X. Yi, and R. Evans, "Optimum design for RF-to-optical up-converter in coherent optical OFDM systems," *IEEE Photon. Technol. Lett*., vol. 19, pp. 483-485, Apr. 2007.

[37] S. L. Jansen, I. Morita, T. C. W. Schenk, and H. Tanaka, "121.9-Gb/s PDM-OFDM transmission with 2-b/s/Hz spectral efficiency over 1000 km of SSMF," *J. Lightwave Technol*., vol. 27, pp. 177-188, Feb. 2009.

[38] C. Sethumadhavan, X. Liu, E. Burrows, and L. Buhl, "Hybrid 107-Gb/s Polarization-multiplexed DQPSK and 42.7-Gb/s DQPSK transmission at 1.4-bits/s/Hz spectral efficiency over 1280 km of SSMF and 4 bandwidth-managed

ROADMs," in European Conference on Optical Communication (ECOC), Paper PD 1.9, pp. 1-2, Sep. 2007.

[39] S. B. Weinstein and P. M. Ebert, "Data transmission by frequency-division multiplexing using the discrete Fourier transform," IEEE *Trans. Commun. Technol*., vol.19, pp. 628-634, Oct. 1971.

[40] L. Hanzo, M. Munster, B. J. Choi, T. Keller, *OFDM and MC-CDMA for Broadband Multi-User Communications, WLANs and Broadcasting*, John Wiley & Sons, 2003.

[41] Communications, WLANs and Broadcasting. New York: Wiley; 2003.

[42] A. J. Lowery, S. Wang and M. Premaratne, "Calculation of power limit due to fiber nonlinearity in optical OFDM systems," *Opt. Express*, vol. 15, pp. 13282-13287, Oct. 2007.

[43] A. J. Lowery, "Fiber nonlinearity mitigation in optical links that use OFDM for dispersion compensation," *IEEE Photon. Technol. Lett*., vol. 19, pp. 1556-1558, Oct. 2007.

[44] A. J. Lowery, "Fiber nonlinearity pre- and post-compensation for long-haul optical links using OFDM," *Opt. Express*, vol. 15, pp. 12965-12970, Oct. 2007.

[45] M. E. Marhic, "Discrete Fourier transforms by single-mode star networks," *Opt. Lett*., vol. 12, pp. 63-65, Jan. 1987.

[46] K. Lee, C. T. D. Thai, and J.-K. K. Rhee, "All optical discrete Fourier transform processor for 100 Gbps OFDM transmission," *Opt. Express*, vol. 16, pp. 4023-4028, Mar. 2008.

[47] G. P. Agrawal, *Nonlinear fiber optics*, 3rd-Ed, Academic Press, 2001.

[48] D. Hillerkuss, A. Marculescu, J. Li, M. Teschke, G. Sigurdsson, K. Worms, S. Ben Ezra, N. Narkiss, W. Freude, and J. Leuthold, "Novel optical fast Fourier transform scheme enabling real-time OFDM processing at 392 Gbit/s and beyond," Optical Fiber Communication Conference (OFC), Paper OWW3, 2010.

[49] D. Hillerkuss, M. Winter, M. Teschke, A. Marculescu, J. Li, G. Sigurdsson, K. Worms, S. Ben Ezra, N. Narkiss, W. Freude, and J. Leuthold, "Simple all-optical FFT scheme enabling Tbit/s real-time signal processing," *Opt. Express*, vol. 18, pp. 9324-9340, Apr. 2010.

[50] K. Shiraishi, T. Sato, and S. Kawakami, "Experimental verification of a form-birefringent polarization splitter," *Appl. Phys. Lett*., vol. 58, pp. 211-212, Jan. 1991.

[51] D. Yi, Y. Yan, H. Liu, S. Lu, and G. Jin, "Broadband polarizing beam splitter based on the form birefringence of a subwavelength grating in the quasi-static domain," *Opt. Lett*., vol. 29, pp. 754-756, Apr. 2004.

[52] Y. Yue, L. Zhang, J.-Y. Yang, R. G. Beausoleil, and A. E. Willner, "Silicon-on-insulator polarization splitter using two horizontally slotted waveguides", *Opt. Lett*., vol. 35, pp. 1364-1366, May 2010.

[53] H. Fukuda, K. Yamada, T. Tsuchizawa, T. Watanabe, H. Shinojima, and S. Itabashi, "Ultrasmall polarization splitter based on silicon wire waveguides," *Opt. Express*, vol. 14, pp. 12401-12408, Dec. 2006.

[54] T. Yamazaki, J. Yamauchi, and H. Nakano, "A branch-type TE/TM wave splitter using a light-guiding metal line," *J. Lightwave Technol*., vol. 25, pp. 922-928, Mar. 2007.

[55] L. Wu, M. Mazilu, J.-F. Gallet, T. F. Krauss, A. Jugessur, and R. M. De La Rue, "Planar photonic crystal polarization splitter," *Opt. Lett*., vol. 29, pp. 1620-1622, Jul. 2004.

[56] M. R. Watts, H. A. Haus, and E. P. Ippen, "Integrated mode-evolution- based polarization splitter," *Opt. Lett*., vol. 30, pp. 967-969, May 2005.

[57] X. Li, G.-R. Zhou, N.-N. Feng, and W. Huang, "A novel planar waveguide wavelength demultiplexer design for integrated optical triplexer transceiver," *IEEE Photon. Technol. Lett*., vol.17, pp. 1214-1216, Jun. 2005.

[58] S. Janz, A. Balakrishnan, S. Charbonneau, P. Cheben, M. Cloutier, A. Delage, K. Dossou, L. Erickson, M. Gao, P.A. Krug, B. Lamontagne, M. Packirisamy, M. Pearson, and D.-X. Xu, "Planar waveguide echelle gratings in silica-on-silicon," *IEEE Photon. Technol. Lett*., vol.16, pp. 503–505, Feb. 2004.

[59] D. C. Flanders, "Submicrometer periodicity gratings as artificial anisotropic dielectrics," *Appl. Phys. Lett*., vol. 42, pp. 492-494, Mar. 1983.

[60] A. Taflove and S. C. Hagness, *Computational electrodynamics: the finite-difference time-domain method*, 3rd-Ed, Artech House Publishers, 2005.

[61] D. M. Sullivan, *Electromagnetic simulation using the FDTD method*, *IEEE Press Series on RF and Microwave Technology*, Wiley-IEEE Press, 2000.

[62] I. H. Malitson, "Interspecimen comparison of the refractive index of fused silica," *J. Opt. Soc. Am.*, vol. 55, pp. 1205-1208, Oct. 1965.

[63] E. D. Palik, *Handbook of optical constants of solids*, vol. I, 1985.

[64] SOPRA N&K Database, http://refractiveindex.info/?group=CRYSTALS&material=a-Si.

[65] J. Chilwell and I. Hodgkinson, "Thin-films field-transfer matrix theory of planar multilayer waveguides and reflection from prism-loaded waveguides," *J. Opt. Soc. Am. A*, vol. 1, pp. 742-753, Jul. 1984.

[66] T. Tamir (Ed), *Guided-wave optoelectronics*, 2nd-Ed, Springer-Verlag, pp. 43-50, 1990.

[67] S. Sinzinger and J. Jahns, *Microoptics*, 2nd-Ed, Wiley-VCH, 2003.

[68] W. -P. Huang and C. L. Xu, "A wide-angle vector beam propagation method," *IEEE Photon. Technol. Lett.*, vol. 4, pp. 1118-1120, Oct. 1992.

[69] F. Marty, L. Rousseau, B. Saadany, B. Mercier, O. Français, Y. Mita, and T. Bourouina, "Advanced etching of silicon based on deep reactive ion etching for silicon high aspect ratio microstructures and three-dimensional micro- and nanostructures," *Microelectronics Journal*, vol. 36, pp. 673–677, Jul. 2005.

[70] Y. Okano, K. Nakagawa, and T. Ito, "Laser mode partition noise evaluation for optical fiber transmission," *IEEE Trans. on Communications*, vol. 28, pp. 238-243, Feb. 1980.

[71] K. Ogawa, "Analysis of mode partition noise in laser transmission systems," *IEEE J. Quantum Electron.*, vol. 18, pp. 849- 855, May 1982.

[72] K. Ogawa and R. Vodhanel, "Measurements of mode partition noise of laser diodes," *IEEE J. Quantum Electron.*, vol. 18, pp. 1090- 1093, Jul. 1982.

[73] P.-L. Liu and K. Ogawa, "Statistical measurements as a way to study mode partition in injection lasers," *J. Lightwave Technol.*, vol. 2, pp. 44- 48, Feb. 1984.

[74] J.C. Campbell, "Calculation of the dispersion penalty for the route design of single-mode systems," *J. Lightwave Technol.*, vol. 6, pp. 564-573, Apr. 1988.

[75] D. Marcuse, "Computer simulation of laser photon fluctuations: Theory of single-cavity laser," *IEEE J. Quantum Electron.*, vol. 20, pp. 1139-1148, Oct. 1984.

[76] D. Marcuse, "Computer simulation of laser photon fluctuations: Single-cavity laser results," *IEEE J. Quantum Electron.*, vol. 20, pp. 1148-1155, Oct. 1984.

[77] L. V. T. Nguyen, "Mode-partition noise in semiconductor lasers", Defense Science and Technology Organization (Australia) research report DSTO-RR-0244, Sep. 2002.

[78] M. Ahmed and M. Yamada, "Influence of instantaneous mode competition on the dynamics of semiconductor lasers," *IEEE J. Quantum Electron.*, vol. 38, pp. 682-693, Jun. 2002.

[79] M. Yamada, W. Ishimori, H. Sakaguchi, and M. Ahmed, "Time-dependent measurement of the mode-competition phenomena among longitudinal modes in long-wavelength lasers," *IEEE J. Quantum Electron.*, vol. 39, pp. 1548-1554, Dec. 2003.

[80] A. M. Yacomotti, L. Furfaro, X. Hachair, F. Pedaci, M. Giudici, J. Tredicce, J. Javaloyes, S. Balle, E. A. Viktorov, and P. Mandel, "Dynamics of multimode semiconductor lasers," *Phys. Rev. A*, vol. 69, 053816, May 2004.

[81] L. Furfaro, F. Pedaci, M. Giudici, X. Hachair, J. Tredicce, and S. Balle, "Mode-Switching in Semiconductor Lasers," *IEEE J. Quantum Electron.*, vol. 40, pp. 1365-1376, Oct. 2004.

[82] G. P. Agrawal, P. J. Anthony, and T.-M. Shen, "Dispersion penalty for 1.3 μm lightwave systems with multimode semiconductor lasers," *J. Lightwave Technol.*, vol. 6, pp. 620-625, May 1988.

[83] N. Cheung, S. Davidow, and D. Duff, "A 90-Mb/s transmission experiment in single-mode fibers using 1.5-μm multi-longitudinal- mode InAsGaP/InP lasers," *J. Lightwave Technol.*, vol. 2, pp. 1034- 1039, Dec. 1984.

[84] R. H. Wentworth, G. E. Bodeep, and T. E. Darcie, "Laser mode partition noise in lightwave systems using dispersive optical fiber," *J. Lightwave Technol.*, vol. 10, pp. 84-89, Jan. 1992.

[85] K. Iwashita and K. Nakagawa, "Mode partition noise characteristics in high-speed modulated laser diodes," *IEEE J. Quantum Electron.*, vol. 18, pp. 2000-2005, Dec. 1982.

[86] T. M. Shen and G. P. Agrawal, "Theoretical analysis of mode partition noise in single-frequency semiconductor lasers," *Electron. Lett.*, vol. 21, pp. 1220-1221, Dec. 1985.

[87] S. Lathi, S. Inoue, S. Kasapi, and Y. Yamamoto, "Longitudinal mode-partition noise in diode lasers," *IEEE Quantum Electronics and Laser Science Conference (QELS)*, pp. 92-93, May 1997.

[88] X. Wang and K. Chan, "Impact of mode partition noise in free-running gain-switched Fabry-Perot laser for 2-dimensional OCDMA," *Opt. Express*, vol. 12, pp. 3334-3340, Jul. 2004.

[89] J. C. Cartledge, "Performance implications of mode partition fluctuations in nearly single longitudinal mode lasers," *J. Lightwave Technol.*, vol. 6, pp. 626-635, May 1988.

[90] J. C. Cartledge and A. F. Elrefaie, "Threshold gain difference requirements for nearly single-longitudinal-mode lasers," *J. Lightwave Technol.*, vol. 8, pp. 704-715, May 1990.

[91] J. C. Cartledge, “On the probabilistic characterization of side mode fluctuations in pulse-modulated nearly-single-mode semiconductor lasers,” *IEEE J. Quantum Electron.*, vol. 26, pp. 2046- 2051, Dec. 1990.

[92] B. R. Clarke, "Mode partition noise introduced by optical filtering," *Electron. Lett.*, vol. 25, pp. 211-212, Feb. 1989.

[93] P. Anandarajah, L. P. Barry, and A. Kaszubowska, "Cross-channel interference due to mode partition noise in WDM optical systems," *Proceedings of 2001 3rd International Conference on Transparent Optical Networks*, pp. 173-176, Jun. 2001.

[94] Z. M. Liao and G. P. Agrawal, "Mode-partition noise in fibre lasers," *Electron. Lett.*, vol. 36, pp. 1188-1189, Jul. 2000.

[95] M. Ramadan, "Parameters affecting mode partition noise in laser transmission systems," *IEEE Global Telecommunications Conference and Exhibition 'Communications Technology for the 1990s and Beyond' (GLOBECOM)*, vol. 2, pp. 692 - 695, Nov. 1989.

[96] C. M. Olsen, K. E. Stubkjaer, and H. Olesen, “Noise caused by semiconductor lasers in high-speed fiber-optic links,” *J. Lightwave Technol.*, vol. 7, pp. 657-665, Apr. 1989.

[97] C. Michie, T. Kelly, and I. Andonovic, "Reflective semiconductor optical amplifiers in passive optical networks," *14th OptoElectronics and Communications Conference (OECC)*, pp. 1-2, Jul. 2009.

[98] K. Sato and H. Toba, "Reduction of mode partition noise by using semiconductor optical amplifiers," *IEEE J. Sel. Topics Quantum Electron.*, vol. 7, no. 2, pp. 328-333, Mar./Apr. 2001.

[99] H.-S. Kim, T. T. Pham, Y.-Y. Won, and S.-K. Han, "Simultaneous wired and wireless 1.25-Gb/s bidirectional WDM-RoF transmission using multiple optical carrier suppression in FP LD," *J. Lightwave Technol.*, vol. 27, pp. 2744-2750, Jul. 2009.

[100] D. Mandridis, I. Ozdur, M. Akbulut and P. J. Delfyett, "A photonic method for overcoming the mode partition noise contribution in the AM Noise spectra of periodic electrical signals," *Conference on Lasers and Electro-Optics (CLEO) and Quantum Electronics and Laser Science Conference (QELS)*, pp. 1-2, May 2010.

[101] S. Pato, P. Monteiro, and H. Silva, "Impact of mode-partition noise in the performance of 10 Gbit/s Ethernet passive optical networks," *9th International Conference on Transparent Optical Networks (ICTON)*, vol. 4, pp.67-70, Jul. 2007.

[102] N. H. Jensen, H. Olesen, and K. E. Stubkjaer, "Partition noise in semiconductor lasers under CW and pulsed operation," *IEEE J. Quantum Electron.*, vol. 23, pp. 71- 80, Jan. 1987.

[103] W. H, Press, S. A. Teukolsky, W. T. Vetterling, and B. P. Flannery, *Numerical Recipes in C*, 2nd-Ed, Cambridge University Press, 1992.